

Damped steady-state resonant sloshing in a circular base container

Raynovskyy I.A.^a, Timokha A.N.^{b,a,*}

^a*Institute of Mathematics of the NAS of Ukraine, Kiev, Tereshchenkivska 3 str., Kiev, 01004, Ukraine*

^b*Centre for Autonomous Marine Operations Systems, Department of Marine Technology, Norwegian University of Science and Technology, NO-74491, Trondheim, Norway*

Abstract

To describe the damped resonant sloshing in a circular base container, the nonlinear modal equations by Faltinsen et al. (2016) are equipped with linear damping terms associated with the logarithmic decrements of the natural sloshing modes. The damping coefficients express a cumulative effect of diverse dissipative phenomena. The surface tension is neglected, the container performs a prescribed periodic sway/surge/pitch/roll motion, the forcing frequency is close to the lowest natural sloshing frequency, and the mean liquid depth - to the tank radius ratio $h \gtrsim 1.2$. An asymptotic steady-state solution of the modal equations is derived; its stability is analysed by the linear Lyapunov method. The dominant amplitudes and the phase-lags of the two primary excited natural sloshing modes are governed by four (secular) nonlinear algebraic equations whose structure is the same as if the container were to perform an elliptic orbital horizontal translatory motion. The steady-state response curves are studied versus the semi-axes ratio of the horizontal elliptic orbit; a line segment (horizontal longitudinal) and a circle (rotary forcing) are two limiting cases. For the longitudinal forcing, planar (standing) and swirling steady-state waves are possible, otherwise, only swirling occurs. A focus is on the phase-lags, which are piecewise functions along the continuous amplitude response curves in the undamped case, but they become of the non-constant character when the damping matters. A comparison is done

*Corresponding author

Email addresses: ihor.raynovskyy@gmail.com (Raynovskyy I.A.),
atimokha@gmail.com, alexander.timokha@ntnu.no (Timokha A.N.)

with measurements of the phase-lag by Royon-Lebeaud et al. (2007) (longitudinal forcing) to show that, if the damping rates are associated with the boundary layer at the wetted tank surface and the bulk viscosity, a satisfactory agreement is established with lower wave amplitudes but the cumulative damping effect must be larger to fit the experiments with increasing amplitudes. For elliptic forcing, stable swirling can be co- or counter-directed with the forcing direction. However, damping makes the counter-directed swirling impossible as the elliptic forcing orbit tends to a circle.

Keywords: Steady-state sloshing, multimodal method, damping, response curves, phase-lags.

1. Introduction

Steady-state resonant nonlinear sloshing in a circular base container caused by harmonic horizontal longitudinal excitations with the forcing frequency close to the lowest natural frequency has been studied by diverse authors, 5 theoretically and experimentally, starting from the 60's. Recent reviews are given by Royon-Lebeaud et al. (2007) and Lukovsky and A.N.Timokha (2017). In analytical studies, viscous damping is normally neglected, which has been supported by experimental data for industrial containers whose geometric dimensions count in metres. However, experimental works by Ikeda 10 et al. (2012), Kim and Kizito (2009), Weheliye et al. (2013), Reclari (2013), Ducci and Weheliye (2014), Reclari et al. (2014) showed that the damping may matter for laboratory tanks (incl. bioreactors) whose horizontal dimension is relatively small. Reasons are the larger viscosity of bioliquid and/or the dynamic contact angle effect (Shukhmurzaev, 1997). Keulegan (1959) 15 showed that the dynamic contact angle effect matters for rectangular tanks with about 15 cm horizontal width and length. Additional dissipative factors can be surface-wave phenomena including contamination and wave breaking (Miles, 1994; Royon-Lebeaud et al., 2007).

For the sway/surge/pitch/roll periodic tank forcing, the most violent resonant sloshing occurs when the forcing frequency is close to the lowest natural 20 sloshing frequency. Faltinsen et al. (2016) studied the undamped steady-state resonant sloshing due to an elliptic type forcing by using the nonlinear multimodal method in the Narimanov–Moiseev approximation. This analytical approach is rather accurate for circular base tanks when the mean 25 liquid depth to the tank radius $h \gtrsim 1.2$. For lower liquid depths, the derived

Narimanov–Moiseev-type modal equations have a limited applicability due to the secondary resonance phenomenon (Faltinsen and Timokha, 2009, Chs. 8, 9). The theoretical steady-state wave regimes, maximum wave elevations and hydrodynamic forces were in satisfactory agreement with experiments including those by Royon-Lebeaud et al. (2007). However, the experimental phase-lag (between the longitudinal sinusoidal forcing and the wave component in the excitation plane) was *not* correctly predicted, even qualitatively, within the framework of the undamped sloshing theory. According to Faltinsen et al. (2016), this phase-lag must be equal to either 0 or π but the measured values were clearly not these constants.

The present paper *accounts for damping* in the Narimanov–Moiseev-type equations by Faltinsen et al. (2016) and constructs the corresponding asymptotic periodic solution to classify the damped resonant steady-state wave regimes.

In § 2, we give the necessary introductory facts about the natural sloshing modes, their frequencies and logarithmic decrements (damping ratios) as well as write down the nonlinear Narimanov–Moiseev-type modal equations by Faltinsen et al. (2016), which couple the free-surface generalised coordinates. The equations are equipped with linear damping terms expressing a cumulative effect of various dissipative phenomena including the boundary layer at the wetted tank surface and the bulk viscosity. The damping ratios caused by the two aforementioned physical factors are theoretically evaluated by Miles and Henderson (1998), asymptotically, in terms of $\delta = \text{Ga}^{-1/4} \ll 1$ where Ga is the Galillei number. The modal equations neglect surface tension (the Bond number $\gtrsim 100$). For tap water, this requires the tank radius $r_0 \gtrsim 0.05$ m.

The Narimanov–Moiseev-type modal equations by Faltinsen et al. (2016) couple the $O(\epsilon^{1/3})$ (dominant), $O(\epsilon^{2/3})$ and $O(\epsilon)$ free-surface generalised coordinates, where $O(\epsilon) \ll 1$ is associated with the nondimensional forcing amplitude. Because these equations neglect the $o(\epsilon)$ terms, the linear damping coefficient ξ_{11} for the two lowest(-order) natural sloshing modes should be of the order $O(\epsilon^{2/3})$ but the linear damping terms for the higher modes can be neglected in our asymptotic analysis.

An analytical asymptotic periodic solution of the modal equations is constructed in § 3.1. Even though arbitrary prescribed sway/surge/roll/pitch periodic tank excitations are postulated, the necessary solvability conditions (secular equations) coupling the lowest-order amplitude components a, \bar{b} and \bar{a}, b ($\sin t$ and $\cos t$ harmonics of the two lowest-order free-surface generalised

coordinates) have the same structure as if the tank performs an elliptic orbital
65 horizontal motion.

The present analysis focuses on the *damped* steady-state wave regimes and their stability, the lowest-order amplitudes $A = \sqrt{a^2 + \bar{a}^2}$, $B = \sqrt{b^2 + \bar{b}^2}$ and the phase-lags ψ , φ versus the semi-axes ratio $0 \leq \delta \leq 1$ of the ‘elliptic’ orbit, whose limit values 0 and 1 correspond to horizontal longitudinal and rotary
70 tank motions, respectively. The secular system has an analytical solution for the undamped case given by Faltinsen et al. (2016), but it does not in the studied case. A possible reason is that ψ and φ are constants when damping is zero, which significantly simplifies the analysis.

In § 3.2, we examine the response curves for the horizontal longitudinal
75 periodic excitations. The damped and undamped amplitude (associated with A and B) response curves are compared to show that damping weakly affects stability ranges of planar standing waves and swirling (steady-state waves existing for this excitation type). The frequency range of irregular waves (chaos) also remains approximately the same as in the undamped case
80 by Faltinsen et al. (2016). In contrast, the phase-lags qualitatively change, becoming complex functions of the forcing frequency and the response amplitude. Measurements of ψ by Royon-Lebeaud et al. (2007) for swirling are used for validation. By assuming the damping rates are basically caused by the boundary layer at the wetted tank surface and the bulk viscosity, a satisfactory consistency is found in a neighbourhood of the primary resonance
85 where the wave amplitude is relatively low. To fit the experimental values of ψ with increasing wave amplitudes, one should increase the damping rates. One reason is a significant wave breaking effect in these experiments.

In § 3.3, we numerically study the response curves associated with A , B
90 and ψ versus the semi-axes ratio of the elliptic forcing orbit. Because the secular system does not have analytical solutions for the studied damped case, a numerical-analytical scheme is adopted. For small non-zero δ , the branching splits so that co-directed (with forcing) swirling belongs to one branch, which has no joint points with another loop-type branch corresponding to the counter-directed swirling. When the forcing orbit tends to a circle ($\delta \rightarrow 1$),
95 the counter-directed swirling disappears so that the rotary (circular) excitations in § 3.4 lead only to co-directed swirling with $A = B$. The response curves are of the hard-spring character as reported by Reclari (2013) and Reclari et al. (2014). Unfortunately, we were not able to compare with the
100 latter experimental measurements because these were done for $h = 1.04$ where the adopted nonlinear modal equations are not applicable due to the

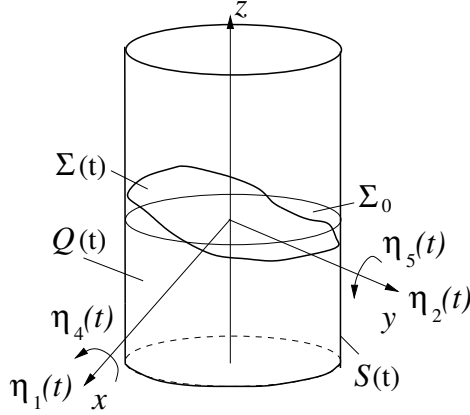


Fig. 1. The liquid domain $Q(t)$ is confined by the free surface $\Sigma(t)$ and the wetted tank surface $S(t)$. Sloshing is considered in the tank-fixed coordinate system $Oxyz$ whose coordinate plane Oxy coincides with the mean (hydrostatic) free surface Σ_0 ; Oz is the symmetry axis. Small-magnitude periodic tank excitations are governed by the generalised coordinates $\eta_1(t)$ (surge), $\eta_4(t)$ (roll), $\eta_2(t)$ (sway), and $\eta_5(t)$ (pitch).

secondary resonance phenomenon.

2. Statement of the problem. Modal equations

An incompressible liquid partly fills an upright circular rigid tank of radius r_0 . The tank performs a small-magnitude prescribed periodic sway/surge/roll/pitch motion, which is furthermore described by the r_0 -scaled periodic generalised coordinates $\eta_1(t)$, $\eta_2(t)$, $\eta_4(t)$ and $\eta_5(t)$ as shown in figure 1. The yaw and heave tank motions are not considered. Figure 1 shows the time-dependent liquid domain $Q(t)$ with the free surface $\Sigma(t)$ (governed by the single-valued function $z = \zeta(r, \theta, t)$) and the wetted tank surface $S(t)$.

Henceforth, the resonant sloshing is studied using a nondimensional statement, which is based on the characteristic size r_0 and time $1/\sigma$, where σ is the circular forcing frequency. A small parameter $0 < \epsilon \ll 1$ is introduced, which is associated with the nondimensional forcing magnitude, i.e. $|\eta_i(t)| = O(\epsilon)$, $i = 1, 2, 4, 5$.

2.1. The natural sloshing modes and frequencies, their damping rates

Linear standing waves in a motionless circular base tank are a superposition of the natural sloshing modes φ_{Mi} , which are the eigenfunctions of the

spectral boundary problem (Faltinsen and Timokha, 2009, Ch. 5)

$$\nabla^2 \varphi_{Mi} = 0 \text{ in } Q_0, \quad \frac{\partial \varphi_{Mi}}{\partial n} = 0 \text{ on } S_0, \quad \frac{\partial \varphi_{Mi}}{\partial n} = \kappa_{Mi} \varphi_{Mi} \text{ on } \Sigma_0, \quad \int_{\Sigma_0} \varphi_{Mi} \, dS = 0, \quad (1)$$

Q_0 is the mean (hydrostatic) liquid domain confined by the mean free surface Σ_0 and the wetted tank surface S_0 (figure 1); σ_{Mi} are the natural sloshing frequencies.

The spectral problem (1) has the analytical solution (Faltinsen and Timokha, 2009, Sect. 4.3.2.2)

$$\varphi_{Mi}(r, \theta, z) = \alpha_{Mi} J_M(k_{Mi} r) \mathcal{Z}_{Mi}(z) \frac{\cos(M\theta)}{\sin(M\theta)}, \quad M = 0, \dots; \quad i = 1, \dots, \quad (2)$$

$$\mathcal{Z}_{Mi}(z) = \frac{\cosh(k_{Mi}(z+h))}{\cosh(k_{Mi}h)}, \quad (3)$$

where $J_M(\cdot)$ is the Bessel function of the first kind, the radial wave numbers k_{Mi} are determined by the transcendental equation $J'_M(k_{Mi}) = 0$, h is the r_0 -scaled mean liquid depth, and we adopt, as in Faltinsen et al. (2016), the normalising multipliers α_{Mi} from the orthogonality condition

$$\alpha_{Mj} \alpha_{Mi} \int_0^1 r J_M(k_{Mi} r) J_M(k_{Mj} r) \, dr = \delta_{ij}, \quad i, j = 1, \dots, \quad (4)$$

where δ_{ij} is the Kronecker delta. The dimensional natural sloshing frequencies are

$$\sigma_{Mi} = \sqrt{\kappa_{Mi} g / r_0}, \quad \kappa_{Mi} = k_{Mi} \tanh(k_{Mi} h), \quad (5)$$

120 where $g = 9.81 \text{ m/s}^2$ is the dimensional gravity acceleration; according to our normalisation, $\bar{\sigma}_{Mi} = \sigma_{Mi} / \sigma$ are the nondimensional sloshing frequencies.

Using this analytical solution and the multimodal method facilitate constructing the analytical solution of any linear sloshing problem in the upright circular cylindrical tank (Faltinsen and Timokha, 2009, Sect. 5.4.4). The derivation suggests the generalised Fourier representations for the free surface and the velocity potential:

$$\begin{aligned} \zeta(r, \theta, t) = & \sum_{M,i}^{I_\theta, I_r} \alpha_{Mi} J_M(k_{Mi} r) \cos(M\theta) p_{Mi}(t) \\ & + \sum_{m,i}^{I_\theta, I_r} \alpha_{mi} J_m(k_{mi} r) \sin(m\theta) r_{mi}(t), \quad (6a) \end{aligned}$$

$$\begin{aligned}
\Phi(r, \theta, z, t) = & \dot{\eta}_1(t) r \cos \theta + \dot{\eta}_2(t) r \sin \theta + F(r, z)[- \dot{\eta}_4(t) \sin \theta + \dot{\eta}_5(t) \cos \theta] \\
& + \sum_{M,i}^{I_\theta, I_r} \alpha_{Mi} J_M(k_{Mi} r) \mathcal{Z}_{Mi}(z) \cos(M\theta) P_{Mi}(t) \\
& + \sum_{m,i}^{I_\theta, I_r} \alpha_{mi} J_m(k_{mi} r) \mathcal{Z}_{mi}(z) \sin(m\theta) R_{mi}(t), \quad (6b)
\end{aligned}$$

where integers $I_\theta, I_r \rightarrow \infty$, $\mathcal{Z}_{Mi}(z)$ are defined by (3) and $F(r, z)$ comes from the so-called linear Stokes-Joukowski potentials, which is reported by Faltinsen et al. (2016) as

$$F(r, z) = rz - \sum_{n=1}^{\infty} \frac{2 P_n}{k_{1n}} J_1(k_{1n} r) \frac{\sinh(k_{1n}(z + \frac{1}{2}h))}{\cosh(\frac{1}{2}k_{1n}h)}; \quad P_n = \int_0^1 r^2 J_1(k_{1n} r) dr. \quad (7)$$

Here, the time-dependent functions $p_{Mi}(t)$ and $r_{mi}(t)$ play the role of the *free-surface generalised coordinates* but $P_{Mi}(t)$ and $R_{mi}(t)$ are interpreted as the *generalised velocities*. All capital summation letters imply changing from zero to I_θ but the lower case indices mean changing from one to either I_θ or I_r . Faltinsen and Timokha (2009, Sect. 5.4.4, eq. (5.155)) showed that the modal solution (6) analytically satisfies the governing Laplace equation and all boundary conditions of the linear sloshing problem, if and only if, the generalised coordinates are, within the framework of the adopted normalisation, the solution of the ordinary differential equations

$$\begin{aligned}
\ddot{p}_{Mi} + \boxed{2\xi_{Mi}\bar{\sigma}_{Mi}\dot{p}_{Mi}} + \bar{\sigma}_{Mi}^2 p_{Mi} &= -\delta_{M1}(\ddot{\eta}_1 - \bar{g}\eta_5 - S_i\ddot{\eta}_5)\kappa_{Mi}P_i, \\
\ddot{r}_{mi} + \boxed{2\xi_{mi}\bar{\sigma}_{mi}\dot{r}_{mi}} + \bar{\sigma}_{11}^2 r_{mi} &= -\delta_{m1}(\ddot{\eta}_2 + \bar{g}\eta_4 + S_i\ddot{\eta}_4)\kappa_{mi}P_i,
\end{aligned} \quad (8)$$

where $\bar{\sigma}_{Mi} = \sigma_{Mi}/\sigma$, $\bar{g} = g/(r_0\sigma^2)$, $S_i = 2 \tanh(k_{Mi}h/2)/k_{Mi}$, and, in addition to Faltinsen and Timokha (2009, eq. (5.155)), we introduced the linear framed damping terms expressing the energy dissipation.

125 According to (8) with the framed terms, the damped free-standing (the right-hand side is zero) waves exponentially decay and the damping ratios ξ_{Mi} are associated with the logarithmic decrements of the natural sloshing modes. Normally, the damping ratios are small nondimensional values. They express a cumulative effect of various dissipative phenomena which are, primarily, the
130 boundary layer at the wetted tank surface and the bulk viscosity (Miles and

Henderson, 1998). For laboratory tanks, additional important dissipative phenomena may be the dynamic contact angle effect (Keulegan, 1959), the free-surface contamination (Miles, 1994) as well as, for violent sloshing, wave breaking (Royon-Lebeaud et al., 2007). When ξ_{Mi} are relatively small, $\bar{\sigma}_{Mi}$ can be accepted equal to those for the undamped case by (5).

Following Miles and Henderson (1998), the damping ratios ξ_{Mi} due to the boundary layer at the wetted tank surface and the bulk viscosity can asymptotically be expressed in terms of the *Galilei number* (Barnyak and Leschuk, 2008), Ga (regarded as a ratio between gravity and viscous forces), or, more precisely, by

$$\delta = Ga^{-1/4} = \sqrt{\nu/(g^{1/2}r_0^{3/2})} \ll 1, \quad (9)$$

where ν is the kinematic viscosity. The lowest-order asymptotic contribution, $\xi_{Mi}^{surf} = O(\delta)$, is associated with the laminar boundary layer on the wetted tank surface; ξ_{Mi}^{surf} is accurately approximated by using the Keulegan analytical technique (Keulegan, 1959). The second-order asymptotic contribution, $\xi_{Mi}^{bulk} = O(\delta^2)$, is due to the bulk viscosity. According to Martel et al. (1998) and Miles and Henderson (1998),

$$\xi_{Mi} = \xi_{Mi}^{surf} + \xi_{Mi}^{bulk} \quad (10)$$

provides a satisfactory agreement with experiments when the aforementioned additional dissipative phenomena are negligible. By adopting an alternative analytical scheme, we re-derived Miles' formulas for the used notations as follows

$$\xi_{Mi}^{surf} = \delta \frac{\mu_{Mi}^{(1)} + \frac{1}{2} J_{Mi}^2(k_{Mi})(\mu_{Mi}^{(2)} + \mu_{Mi}^{(3)})}{2\sqrt{2} \kappa_{Mi}^{5/4} \mu_{Mi}^{(0)}}, \quad (11a)$$

$$\xi_{Mi}^{bulk} = \delta^2 \left[\frac{2k_{Mi}^2}{\kappa_{Mi}^{1/2}} - \frac{J_{Mi}^2(k_{Mi}) \mu_{Mi}^{(2)}}{2\kappa_{Mi}^{3/2} \mu_{Mi}^{(0)}} \right], \quad (11b)$$

where

$$\begin{aligned}
\mu_{Mi}^{(0)} &= \int_0^1 r J_{Mi}^2(k_{Mi}r) dr, \quad \mu_{Mi}^{(1)} = \int_0^1 r k_{Mi}^2 J_{Mi}'^2(k_{Mi}r) dr + M^2 \int_0^1 \frac{J_{Mi}^2(k_{Mi}r)}{r} dr, \\
\mu_{Mi}^{(2)} &= M^2 \left(\frac{\tanh(k_{Mi}h)}{k_{Mi}} + \frac{h}{\cosh^2(k_{Mi}h)} \right), \\
\mu_{Mi}^{(3)} &= k_{Mi}^2 \left(\frac{\tanh(k_{Mi}h)}{k_{Mi}} - \frac{h}{\cosh^2(k_{Mi}h)} \right).
\end{aligned} \tag{12}$$

Whereas the Galileo number $\text{Ga} = gr_0^3/\nu^2$ is regarded as a ratio between gravity and viscous forces, the Bond number $\text{Bo} = \rho gr_0^2/T_s$ (ρ is the liquid density and T_s is the surface tension) expresses the ratio of gravitational forces to surface tension forces. The surface tension can be neglected when
140 $100 \lesssim \text{Bo}$ (Faltinsen and Timokha, 2009, Ch. 4). For tap water at Earth conditions with $\rho = 10^3 \text{ kg/m}^3$ and $T_s = 0.073 \text{ N/m}$, this inequality leads to $0.05 \text{ m} \lesssim r_0$. Because the Narimanov-Moiseev-type model equations by Faltinsen et al. (2016) neglect surface tension, the forthcoming analysis implicitly assumes the later restriction on r_0 .

145 2.2. The Narimanov-Moiseev-type modal equations

Faltinsen et al. (2016) used the nonlinear multimodal method to derive a system of nonlinear ordinary differential equations (instead of (8)), which describes the resonant sloshing in a circular base tank when the forcing frequency is close to the lowest natural sloshing frequency, the sway/surge/roll/
150 pitch magnitude is small relative to the tank radius, and there are no secondary resonances ($h \gtrsim 1.2$).

Using the Bateman-Luke variational formalism (Ch. 7 by Faltinsen and Timokha, 2009), the modal representation (6), assumptions of the Narimanov-Moiseev-type asymptotic theory

$$\begin{aligned}
p_{11} \sim r_{11} &= O(\epsilon^{1/3}), \quad p_{0j} \sim p_{2j} \sim r_{2j} = O(\epsilon^{2/3}), \\
r_{1(j+1)} \sim p_{1(j+1)} \sim p_{3j} \sim r_{3j} &= O(\epsilon), \quad j = 1, 2, \dots, I_r; \quad I_r \rightarrow \infty
\end{aligned} \tag{13a}$$

$$\bar{\sigma}_{11}^2 - 1 = O(\epsilon^{2/3}), \quad \bar{\sigma}_{Mi} = \sigma_{Mi}/\sigma, \tag{13b}$$

Faltinsen et al. (2016) obtained the following nonlinear approximate modal equations of the Narimanov-Moiseev type with respect to the free-surface generalised coordinates

$$\ddot{p}_{11} + \boxed{2\xi_{11}\bar{\sigma}_{11}\dot{p}_{11}} + \bar{\sigma}_{11}^2 p_{11} + \mathcal{P}_{11}(p_{11}, r_{11}; p_{0j}, p_{2j}, r_{2j}) = -(\ddot{\eta}_1 - \bar{g}\eta_5 - S_1\ddot{\eta}_5)\kappa_{11}P_1, \quad (14a)$$

$$\ddot{r}_{11} + \boxed{2\xi_{11}\bar{\sigma}_{11}\dot{r}_{11}} + \bar{\sigma}_{11}^2 r_{11} + \mathcal{R}_{11}(p_{11}, r_{11}; p_{0j}, p_{2j}, r_{2j}) = -(\ddot{\eta}_2 + \bar{g}\eta_4 + S_1\ddot{\eta}_4)\kappa_{11}P_1; \quad (14b)$$

$$\ddot{p}_{2k} + \boxed{2\xi_{2k}\bar{\sigma}_{2k}\dot{p}_{2k}} + \bar{\sigma}_{2k}^2 p_{2k} + \mathcal{P}_{2k}(p_{11}, r_{11}) = 0, \quad (15a)$$

$$\ddot{r}_{2k} + \boxed{2\xi_{2k}\bar{\sigma}_{2k}\dot{r}_{2k}} + \bar{\sigma}_{2k}^2 r_{2k} + \mathcal{R}_{2k}(p_{11}, r_{11}) = 0, \quad (15b)$$

$$\ddot{p}_{0k} + \boxed{2\xi_{0k}\bar{\sigma}_{0k}\dot{p}_{0k}} + \bar{\sigma}_{0k}^2 p_{0k} + \mathcal{P}_{0k}(p_{11}, r_{11}) = 0; \quad (15c)$$

$$\ddot{p}_{3k} + \boxed{2\xi_{3k}\bar{\sigma}_{3k}\dot{p}_{3k}} + \bar{\sigma}_{3k}^2 p_{3k} + \mathcal{P}_{3k}(p_{11}, r_{11}; p_{0j}, p_{2j}, r_{2j}) = 0, \quad (16a)$$

$$\ddot{r}_{3k} + \boxed{2\xi_{3k}\bar{\sigma}_{3k}\dot{r}_{3k}} + \bar{\sigma}_{3k}^2 r_{3k} + \mathcal{R}_{3k}(p_{11}, r_{11}; p_{0j}, p_{2j}, r_{2j}) = 0, \quad k = 1, \dots, I_r; \quad (16b)$$

$$\ddot{p}_{1n} + \boxed{2\xi_{1n}\bar{\sigma}_{1n}\dot{p}_{1n}} + \bar{\sigma}_{1n}^2 p_{1n} + \mathcal{P}_{1n}(p_{11}, r_{11}; p_{0j}, p_{2j}, r_{2j}) = -(\ddot{\eta}_1 - \bar{g}\eta_5 - S_n\ddot{\eta}_5)\kappa_{1n}P_n, \quad (17a)$$

$$\ddot{r}_{1n} + \boxed{2\xi_{1n}\bar{\sigma}_{1n}\dot{r}_{1n}} + \bar{\sigma}_{1n}^2 r_{1n} + \mathcal{R}_{1n}(p_{11}, r_{11}; p_{0j}, p_{2j}, r_{2j}) = -(\ddot{\eta}_2 + \bar{g}\eta_4 + S_n\ddot{\eta}_4)\kappa_{1n}P_n, \quad (17b)$$

$n = 2, \dots, I_r$, where the nonlinear terms \mathcal{P}_{Mi} , \mathcal{R}_{mi} are presented in Appendix A. We also see that only generalised coordinates with $M = 0, 1, 2, 3$ are included into the modal equations. The generalised coordinates with $M, m \geq 4$ are described by homogeneous linear modal equations from (8); these generalised coordinates are not excited and, therefore, do not contribute on the long-time scale due to the damping. The system of ordinary differential equations needs either initial or periodicity conditions. The latter describes the steady-state wave regimes.

160 Specifically, the third-order generalised coordinates in (16), (17) are 'driven',
namely, p_{3n} , r_{3n} , $r_{1(n+1)}$, $p_{1(n+1)}$, $n \geq 1$ are not present in other equations
and only linearly included in (16), (17). This means that with a solution of
(14), (15), one can easily derive the aforementioned driven generalised coordi-
nates. The focus should therefore be on (14), (15) where only equations
165 (14) contain the forcing (non-zero right-hand side).

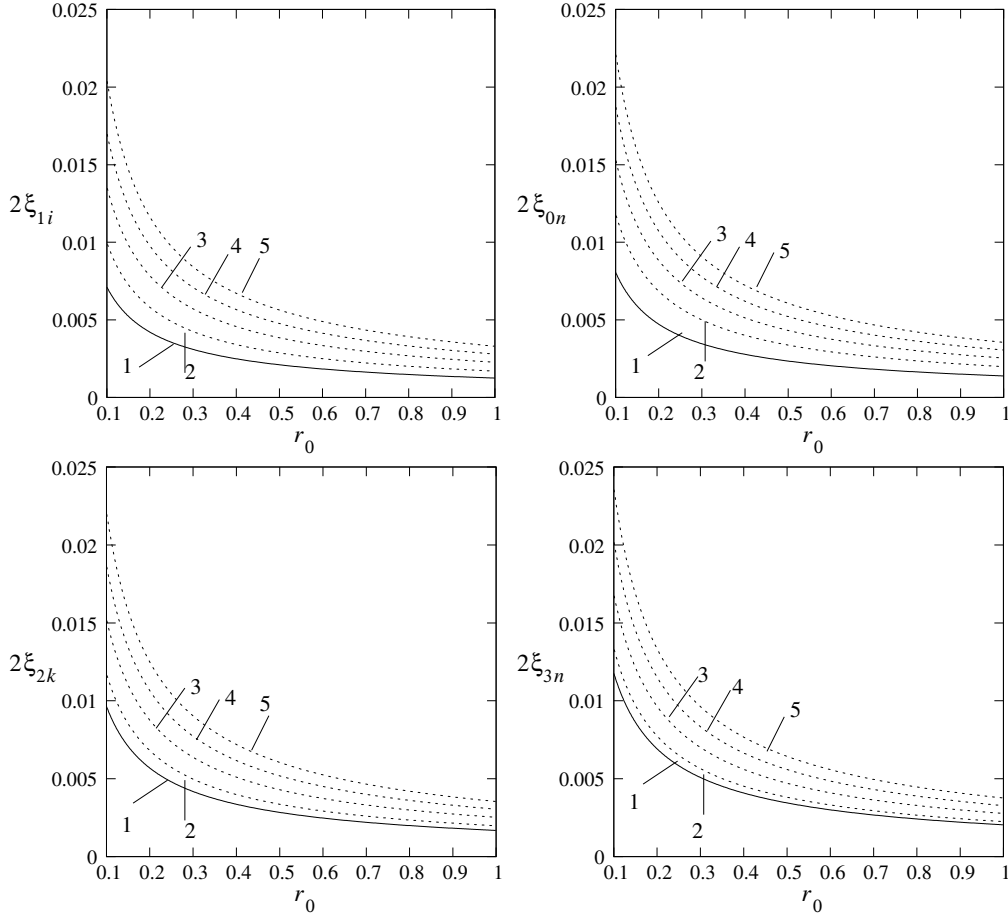


Fig. 2. The theoretical damping rates $2\xi_{Mi}$ by (10)–(12) for $M = 0, 1, 2, 3$. Tap water with $\nu = 10^{-6} \text{ m}^2/\text{s}$ and $g = 9.81 \text{ m/s}^2$. The second index is used to mark the curves.

A *novelty* consists of the framed linear damping terms, which were not considered by Faltinsen et al. (2016). Because the Narimanov-Moiseev-type equations have an asymptotic character suggesting (13a) for the free-surface

generalised coordinates and neglecting the $o(\epsilon)$ terms, including the framed terms into (14)–(17) implies, implicitly,

$$\xi_{11} = O(\epsilon^{2/3}), \quad \xi_{2i} \sim \xi_{0i} \sim \xi_{3i} \sim \xi_{1n} = O(1), \quad i \geq 1, n \geq 2, \quad (18)$$

where the order $O(1)$ for the higher-order generalised coordinates looks unphysical and inconsistent with our assumptions that the damping rates are small non-dimensional parameters.

Let us suggest that the damping ratios are basically contributed by the boundary layer at the wetted tank surface and the bulk viscosity and are numerically evaluated by (10), (11) for tap water versus the tank radius r_0 . The result is presented in figure 2. It shows that all these damping rates are indeed small parameters tending to zero with increasing r_0 . A particular conclusion is that this kind of damping (boundary layer and bulk viscosity) can be neglected for large industrial tanks. However, for smaller r_0 (laboratory containers), the damping ratio $\xi_{11} = O(\epsilon^{2/3})$ should most probably be accounted for in the sloshing analysis, especially, if we assume that the above-discussed additional dissipative factors (dynamic contact angle, contamination, wave breaking, etc.) may sufficiently increase ξ_{11} relative to its estimate (from below) by (10), (11).

3. Asymptotic periodic solution and steady-state wave regimes

3.1. Steady-state (periodic) solution and its stability

We assume an arbitrary sway/surge/pitch/roll periodic tank forcing of the order $O(\epsilon)$, i.e.,

$$\eta_i(t) = \sum_{k=1}^{\infty} \left[\eta_{ia}^{(k)} \cos(kt) + \mu_{ia}^{(k)} \sin(kt) \right], \quad \eta_{ia}^{(k)} \sim \mu_{ia}^{(k)} = O(\epsilon), \quad (19)$$

where the lowest-order Fourier harmonics are not zero, i.e.

$$\sum_{i=1,2,4,5} |\eta_{ia}^{(1)}| + |\mu_{ia}^{(1)}| \neq 0. \quad (20)$$

When discussing the Narimanov-Moiseev-type equations, we pointed out that one can omit the driven generalised coordinates but focus on the subsystem (14), (15) where only two equations (14) have a non-zero right-hand

side. Substituting (19) into these right-hand sides gives

$$\begin{aligned}
& P_1 \kappa_{11} \sum_{k=1}^{\infty} \left[(k\eta_{1a}^{(k)} - (kS_1 - \bar{g})\eta_{5a}^{(k)}) \cos(kt) + (k\mu_{1a}^{(k)} - (kS_1 - \bar{g})\mu_{5a}^{(k)}) \sin(kt) \right], \\
& P_1 \kappa_{11} \sum_{k=1}^{\infty} \left[(k\eta_{2a}^{(k)} + (kS_1 - \bar{g})\eta_{4a}^{(k)}) \cos(kt) + (k\mu_{2a}^{(k)} + (kS_1 - \bar{g})\mu_{4a}^{(k)}) \sin(kt) \right],
\end{aligned} \tag{21}$$

in which, due to the Moiseev detuning condition (13b), neglecting the $o(\epsilon)$ terms replaces $\bar{g} = g/(r_0\sigma^2) \rightarrow \bar{g} = g/(r_0\sigma_{11}^2)$.

Furthermore, because of the Narimanov-Moiseev approximation (13), in which only the first harmonics, being of the order $O(\epsilon)$, excites the $O(\epsilon^{1/3})$ order components while the others contribute $O(\epsilon)$, one can concentrate on the amplitudes at the lowest harmonics, $\cos t$ and $\sin t$, in (14a) and (14b):

$$\begin{aligned}
\epsilon_x &= P_1 \kappa_{11} (\eta_{1a}^{(1)} - [S_1 - \bar{g}]\eta_{5a}^{(1)}), \quad \bar{\epsilon}_x = P_1 \kappa_{11} (\mu_{1a}^{(1)} - [S_1 - \bar{g}]\mu_{5a}^{(1)}), \\
\bar{\epsilon}_y &= P_1 \kappa_{11} (\eta_{2a}^{(1)} + [S_1 - \bar{g}]\eta_{4a}^{(1)}), \quad \epsilon_y = P_1 \kappa_{11} (\mu_{2a}^{(1)} + [S_1 - \bar{g}]\mu_{4a}^{(1)}),
\end{aligned} \tag{22}$$

185 where ϵ_x and $\bar{\epsilon}_x$ imply the lowest-harmonic forcing components in the Ox direction, but $\bar{\epsilon}_y$ and ϵ_y correspond to the $\cos t$ and $\sin t$ harmonics along the Oy axis.

An *important fact* is that the same $\cos t$ and $\sin t$ right-hand sides in (14a) and (14b) appear when the tank performs the horizontal translatory motion

$$\begin{aligned}
\eta_1(t) &= -\hat{\eta}_{1a}^{(c)} \cos t - \hat{\eta}_{1a}^{(s)} \sin t \\
&= -(\eta_{1a}^{(1)} - [S_1 - \bar{g}]\eta_{5a}^{(1)}) \cos t - (\mu_{1a}^{(1)} - [S_1 - \bar{g}]\mu_{5a}^{(1)}) \sin t,
\end{aligned} \tag{23a}$$

$$\begin{aligned}
\eta_2(t) &= -\hat{\eta}_{2a}^{(c)} \cos t - \hat{\eta}_{2a}^{(s)} \sin t \\
&= -(\eta_{2a}^{(1)} + [S_1 - \bar{g}]\eta_{4a}^{(1)}) \cos t - (\mu_{2a}^{(1)} + [S_1 - \bar{g}]\mu_{4a}^{(1)}) \sin t.
\end{aligned} \tag{23b}$$

This artificial translatory tank motion occurs along an *elliptic* trajectory in the Oxy plane, clock- or counterclockwise. Without loss of generality, one can focus on the counterclockwise case. Furthermore, using a time phase-shift $t := t + t_1$ and rotating Oxy around the cylinder axis (the major semi-axis of the elliptic orbit should coincide with Ox) make it possible to arrive at

$$\epsilon_x > 0, \quad \epsilon_y \geq 0, \quad \bar{\epsilon}_y = \bar{\epsilon}_x = 0 \tag{24}$$

in (22). We assume that (24) is *satisfied* in the forthcoming analysis. *Physically*, this means that, without loss of generality, we concentrate on elliptic counterclockwise horizontal tank excitations by (23) with the major semi axis $\hat{\eta}_{1a}^{(c)} = \eta_{1a} \ll 1$ belonging to the Ox axis and the minor semi-axis $\hat{\eta}_{2a}^{(s)} = \eta_{2a} \ll 1$ ($\hat{\eta}_{1a}^{(s)} = \hat{\eta}_{2a}^{(c)} = 0$). 190

To find an asymptotic steady-state solution of the modal equations, we use the Bubnov–Galerkin procedure by Faltinsen et al. (2016) by posing the lowest-order components of the primary excited modes as

$$p_{11}(t) = a \cos t + \bar{a} \sin t + O(\epsilon), \quad r_{11}(t) = \bar{b} \cos t + b \sin t + O(\epsilon), \quad (25)$$

where the nondimensional amplitude parameters a, \bar{a}, \bar{b} , and b have the lowest order $O(\epsilon^{1/3})$. Inserting (25) into (15) yields the second-order generalised coordinates

$$p_{0k}(t) = s_{0k}(a^2 + \bar{a}^2 + b^2 + \bar{b}^2) + s_{1k} [(a^2 - \bar{a}^2 - b^2 + \bar{b}^2) \cos 2t + 2(a\bar{a} + b\bar{b}) \sin 2t] + o(\epsilon), \quad (26a)$$

$$p_{2k}(t) = c_{0k}(a^2 + \bar{a}^2 - b^2 - \bar{b}^2) + c_{1k} [(a^2 - \bar{a}^2 + b^2 - \bar{b}^2) \cos 2t + 2(a\bar{a} - b\bar{b}) \sin 2t] + o(\epsilon), \quad (26b)$$

$$r_{2k}(t) = 2c_{0k}(a\bar{b} + b\bar{a}) + 2c_{1k} [(a\bar{b} - b\bar{a}) \cos 2t + (ab + \bar{a}\bar{b}) \sin 2t] + o(\epsilon), \quad (26c)$$

where

$$\begin{aligned} s_{0k} &= \frac{1}{2} \left(\frac{d_{10,k} - d_{8,k}}{\bar{\sigma}_{0k}^2} \right), & s_{1k} &= \frac{d_{10,k} + d_{8,k}}{2(\bar{\sigma}_{0k}^2 - 4)}, \\ c_{0k} &= \frac{1}{2} \left(\frac{d_{9,k} - d_{7,k}}{\bar{\sigma}_{2k}^2} \right), & c_{1k} &= \frac{d_{9,k} + d_{7,k}}{2(\bar{\sigma}_{2k}^2 - 4)}, \end{aligned} \quad (27)$$

but substituting (25) and (26) into (14), (16) and (17) gives the actual periodic asymptotic solution of the model equations (Faltinsen et al., 2016).

Gathering the first harmonic terms, $\cos t$ and $\sin t$, in (14) yields the *necessary solvability* condition appearing as the following (secular) system of

nonlinear algebraic equations

$$\begin{cases} \textcircled{1} : a [(\bar{\sigma}_{11}^2 - 1) + m_1(a^2 + \bar{a}^2 + \bar{b}^2) + m_3b^2] + \bar{a}[(m_1 - m_3)\bar{b}b + \xi] = \epsilon_x, \\ \textcircled{2} : \bar{a} [(\bar{\sigma}_{11}^2 - 1) + m_1(a^2 + \bar{a}^2 + b^2) + m_3\bar{b}^2] + a[(m_1 - m_3)\bar{b}b - \xi] = 0, \\ \textcircled{3} : b [(\bar{\sigma}_{11}^2 - 1) + m_1(b^2 + \bar{b}^2 + \bar{a}^2) + m_3a^2] + \bar{b}[(m_1 - m_3)\bar{a}a - \xi] = \epsilon_y, \\ \textcircled{4} : \bar{b} [(\bar{\sigma}_{11}^2 - 1) + m_1(b^2 + \bar{b}^2 + a^2) + m_3\bar{a}^2] + b[(m_1 - m_3)\bar{a}a + \xi] = 0 \end{cases} \quad (28)$$

with respect to a, \bar{a}, \bar{b} and b ; here, $\xi = 2\xi_{11}$, coefficients m_1 and m_3 are computed by the formulas

$$m_1 = -\frac{1}{2}d_1 + \sum_{j=1}^{I_r} \left[c_{1j} \left(\frac{1}{2}d_3^{(j)} - 2d_4^{(j)} \right) + s_{1j} \left(\frac{1}{2}d_5^{(j)} - 2d_6^{(j)} \right) - s_{0j}d_5^{(j)} - c_{0j}d_3^{(j)} \right], \quad (29a)$$

$$m_3 = \frac{1}{2}d_1 - 2d_2 + \sum_{j=1}^{I_r} \left[c_{1j} \left(\frac{3}{2}d_3^{(j)} - 6d_4^{(j)} \right) + s_{1j} \left(-\frac{1}{2}d_5^{(j)} + 2d_6^{(j)} \right) - s_{0j}d_5^{(j)} + c_{0j}d_3^{(j)} \right] \quad (29b)$$

195 and are functions of h and the nondimensional forcing frequency $\bar{\sigma}_{11}$. Utilising (13b) shows that the latter dependence can be neglected by substituting $\sigma = \sigma_{11}$ into (29). Dependence on σ remains only in the $(\bar{\sigma}_{11}^2 - 1)$ -quantity of (28). Specifically, repeating the previous derivations with accounting for all Fourier harmonics of (21) will lead to the same secular equations (28),
 200 namely, the higher harmonics do not affect the solvability (secularity) condition but may only slightly correct the highest-order components of the steady-state waves.

One should remark that, according to the lowest-order approximation (25), the free-surface steady-state waves are defined as the superposition of the two out-of-phase angular modes,

$$\zeta(r, \theta, t) = J_1(k_{11}r) \left[(a \cos \theta + \bar{b} \sin \theta) \cos t + (\bar{a} \cos \theta + b \sin \theta) \sin t \right] + o(\epsilon^{2/3}), \quad (30)$$

which determines a *swirling* wave (angular progressive wave, see definition of swirling in Faltinsen and Timokha, 2009) unless $(a \cos \theta + \bar{b} \sin \theta)$ and $(\bar{a} \cos \theta + b \sin \theta)$ constitute two congruent patterns, which happens, if and only if,

$$ab = \bar{a}\bar{b}. \quad (31)$$

The condition (31) means that a *standing* steady-state wave occurs.

Our main task consists of *classifying* the steady-state wave regimes which means description of when stable/unstable standing/swirling waves are re-
 205 realised and what is the direction (clock- or counterclockwise) of swirling. The linear Lyapunov method and the multi-timing technique is employed to study stability of the constructed asymptotic steady-state solution as described in Appendix B.

For (28) with $\xi = 0$ (damping is neglected), Faltinsen et al. (2016) proved that $\bar{a} = \bar{b} = 0$ for $0 \leq \epsilon_y/\epsilon_x < 1$ and showed how to find analytically a and b . As long as $\xi \neq 0$, the amplitude parameters \bar{a} and \bar{b} are generally not zero and, therefore, this solution method cannot be extended to the damped sloshing. Following Faltinsen and Timokha (2017), we rewrite (28) in a more physically-relevant form in terms of the integral lowest-order amplitudes A, B and the phase-lags ψ, φ defined by

$$A = \sqrt{a^2 + \bar{a}^2} \quad \text{and} \quad B = \sqrt{b^2 + \bar{b}^2} > 0, \quad (32a)$$

$$a = A \cos \psi, \quad \bar{a} = A \sin \psi, \quad \bar{b} = B \cos \varphi, \quad b = B \sin \varphi. \quad (32b)$$

Inserting (32) into expressions \bar{a} ① $- a$ ②, \bar{b} ③ $- b$ ④, a ① $+ \bar{a}$ ② and b ③ $+ \bar{b}$ ④ of (28) yields the following alternative secular equations

$$\begin{cases} \boxed{1} : A[\Lambda + m_1 A^2 + (m_3 - \mathcal{F})B^2] = \epsilon_x \cos \psi, & \boxed{3} : A[\mathcal{D}B^2 + \xi] = \epsilon_x \sin \psi, \\ \boxed{2} : B[\Lambda + m_1 B^2 + (m_3 - \mathcal{F})A^2] = \epsilon_y \sin \varphi, & \boxed{4} : B[\mathcal{D}A^2 - \xi] = \epsilon_y \cos \varphi, \end{cases} \quad (33a)$$

$$\begin{aligned} \mathcal{F} &= (m_3 - m_1) \cos^2(\alpha) = (m_3 - m_1)/(1 + C^2), \\ \mathcal{D} &= (m_3 - m_1) \sin(\alpha) \cos(\alpha) = (m_3 - m_1) C/(1 + C^2), \end{aligned} \quad (33b)$$

where

$$\Lambda = \bar{\sigma}_{11}^2 - 1, \quad \alpha = \varphi - \psi, \quad C = \tan \alpha, \quad 0 \leq \epsilon_y \leq \epsilon_x \neq 0,$$

210 ($\mathcal{F}(\alpha)$ and $\mathcal{D}(\alpha)$ are the π -periodic functions of the phase-lag difference α). The secular systems (28) and (33) are *mathematically equivalent*, i.e., getting known A, B, ψ, φ from (33) determines a, \bar{a}, b, \bar{b} and *vice versa*.

In terms of (32) and (33), when $AB > 0$, the standing wave condition (31) is equivalent to

$$\sin \alpha = 0 \quad \Leftrightarrow \quad C = 0. \quad (34)$$

3.2. Longitudinal periodic tank excitations along the Ox axis ($\epsilon_y = 0$)

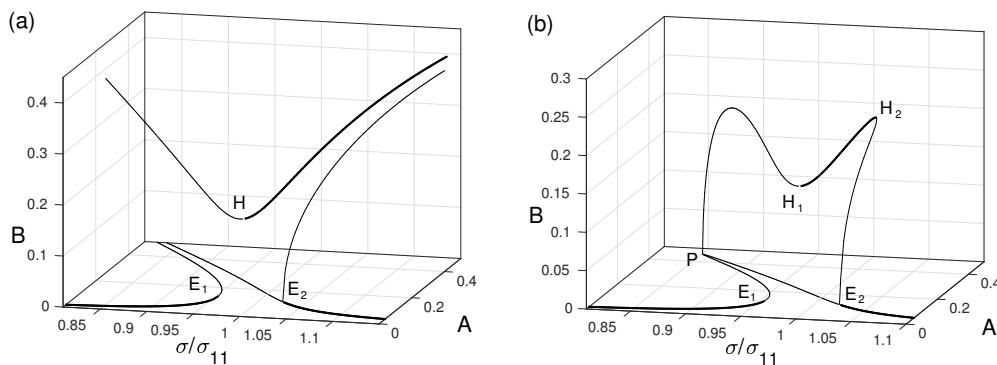


Fig. 3. The wave amplitude response curves in the $(\sigma/\sigma_{11}, A, B)$ -space for the longitudinal horizontal forcing in the Oxz -plane, $h = 1.5$, the nondimensional forcing amplitude $\eta_{1a} = 0.01$ ($\eta_{2a} = 0$). The branches are computed by using (35) for planar ($B = 0$) and (36) is used for swirling ($B > 0$) waves. The bold lines mark stable solutions. The undamped sloshing ($\xi = 0$) is presented in (a) and the damped case with $\xi = 0.02$ is shown in (b). There is no stable steady-state sloshing between E_1 and E_2 where irregular (chaotic) waves are predicted. Curves belonging to the $(\sigma/\sigma_{11}, A)$ plane correspond to the planar steady-state wave regime. The non-zero damping causes the response curves, which do not go to infinity due to the bifurcation point P , where swirling emerges from the planar wave branching, and H_2 , which restricts swirling to finite amplitudes when following along the H branch with increasing σ/σ_{11} .

The undamped ($\xi = 0$) steady-state sloshing for the longitudinal harmonic forcing ($\epsilon_y = 0$) was analysed by Faltinsen et al. (2016). They mathematically proved that $\epsilon_y = \xi = 0 \Rightarrow \bar{a} = \bar{b} = 0$ and there exist two physically-different steady-state solutions of the modal system corresponding to *planar* standing ($b = 0$ and (31) is satisfied) and *swirling* ($ab \neq 0$ in (31)) waves. In terms of definitions (32) and (33) with $\xi = 0$, the planar steady-state waves imply $A > 0$, $B = 0$, $\sin \psi = 0$, $C = 0$ (the phase-lag φ is not defined) but swirling means $AB > 0$, $\sin \psi = \cos \varphi = 0$ ($C = \pm\infty$). Swirling consists of two identical angular progressive waves occurring in either counter- or clockwise directions, the directions correspond to $C = +\infty$ and $-\infty$ ($\alpha = \pi/2$ and $\alpha = -\pi/2$), respectively.

When $\xi > 0$, (33) has physically the same solutions. The *planar* standing wave corresponds to $B = 0$, $A > 0$ and $C \neq 0$. The phase-lag ψ (φ is not

defined) is *not* a piecewise function anymore. Using $\boxed{1}^2 + \boxed{3}^2 =$

$$= A^2 [(\Lambda + m_1 A^2)^2 + \xi^2] = \epsilon_x^2; \quad 0 < A \leq \frac{\epsilon_x}{\xi}; \quad \psi = \arccos \frac{A(\Lambda + m_1 A^2)}{\epsilon_x}, \quad (35)$$

gives the necessary expressions for computing A and ψ . The steady-state *swirling* suggests $AB > 0$, $C \neq 0$, which can be computed by rewriting (33) in the form

$$\begin{cases} A \left[\Lambda + m_1 A^2 + \frac{m_1 + m_3 C^2}{1 + C^2} B^2 \right] = \epsilon_x \cos \psi; \\ A \left[\frac{(m_3 - m_1)C}{1 + C^2} B^2 + \xi \right] = \epsilon_x \sin \psi; \\ B^2 = -\frac{1}{m_1} \left[\Lambda + \frac{m_1 + m_3 C^2}{1 + C^2} A^2 \right] > 0; \quad A^2 = \frac{\xi (1 + C^2)}{(m_3 - m_1)C} > 0, \end{cases} \quad (36)$$

where

$$P_l(C) = q_3 C^3 + q_2 C^2 + q_1 C + q_0 = 0, \quad (37)$$

with

$$\begin{aligned} q_3 &= \xi^3 (m_1 + m_3)^2 > 0, \quad q_2 = 2\xi^2 \Lambda (m_3^2 - m_1^2), \\ q_1 &= \xi [4\xi^2 m_1^2 + \Lambda^2 (m_1 - m_3)^2], \quad q_0 = \epsilon_x^2 m_1^2 (m_1 - m_3). \end{aligned}$$

225 Illustrative response curves for the undamped (a) and damped (b) steady-state sloshing are shown in figure 3. The computations were made with $h = 1.5$, the forcing amplitude is $\eta_{1a} = 0.01$ ($\eta_{3a} = \eta_{2a} = \eta_{4a} = 0$), and the damping coefficient $\xi = 2\xi_{11} = 0.02$. Choosing this value of ξ suggests $0.05 \text{ m} \leq r_0 \leq 0.1 \text{ m}$, the boundary layer and bulk viscosity damping effect and, possibly, a non-negligible contribution of dissipative phenomena
230 mentioned above.

The branching in figure 3 is computed by using (35) for planar waves ($B = 0$), and (36) is used for swirling ($B > 0$). The branches belonging to the $(\sigma/\sigma_{11}, A)$ plane are responsible for planar waves. The bold lines mark
235 stable solutions. We see that the stable planar standing-wave sloshing is expected to the left of E_1 and to the right of E_2 ; it becomes unstable in a neighbourhood of the primary resonance $\sigma/\sigma_{11} = 1$ where stable swirling (to the right of H [H_1]) and irregular waves (there is no stable steady-state sloshing) between E_1 and H [H_1] are predicted. Direct numerical simulations

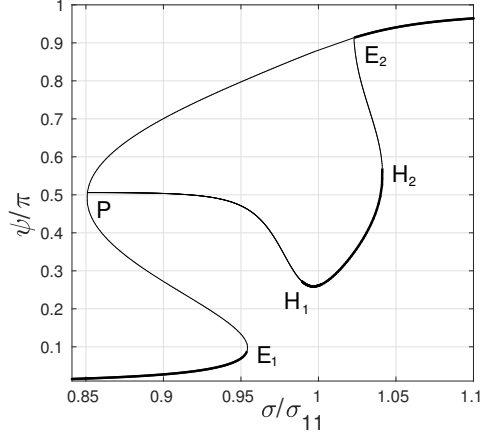


Fig. 4. The same as in figure 3 (b) but for the phase-lag ψ/π . When $\xi = 0$, ψ/π takes the two discrete values 0 and 1 depending on the steady-state wave regime and the forcing frequency σ/σ_{11} .

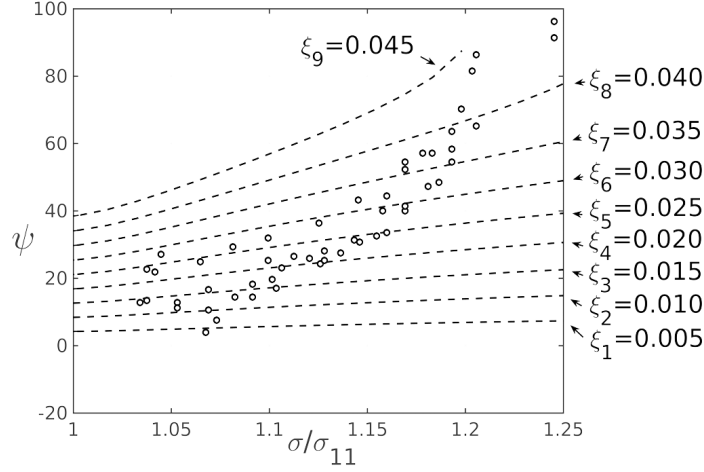


Fig. 5. Experimental values of ψ by Royon-Lebeaud et al. (2007) (marked by circles) for stable swirling (correspond to the subbranch H_1H_2 in figure 3 b) and their theoretical predictions made with different $\xi = \xi_i$ starting from the lower bound $\xi_1 = 0.005$ by (10) and (11); $h = 1.5$ and $\eta_{1a} = 0.045$, $\eta_{2a} = 0$ (the longitudinal horizontal harmonic forcing). The comparison shows that the actual damping rate increases with the wave amplitude response (along H_1H_2) that can be explained by additional dissipative factors (Royon-Lebeaud, Hopfinger and Cartellier, 2007, reported a strong wave breaking).

240 and experimental observations on what happens in those zones of instability are discussed, e.g. by Miles (1984a,b) and Ikeda et al. (2012) but not for elliptic forcing. Due to the damping effect, the stable swirling frequency range has an upper bound associated with H_2 .

The undamped response curves in figure 3 (a) were already discussed
 245 by Faltinsen et al. (2016). Figure 3 (b) shows that a non-zero ξ removes infinitely-located points on this branching but stability ranges of planar waves and swirling are weakly affected by $\xi = 0.02$ so that positions of E_1, E_2 and H_1 (replaces H) determining these ranges remain almost the same. This explains the good agreement with experiments on the stability ranges estab-
 250 lished using the undamped model. A novelty in (b) is two points H_2 and P , which can be treated as bifurcation points where swirling emerges from the planar standing-wave sloshing. The swirling branching constitutes an arc, which is pinned at P and E_1 ; its stable subbranch H_1H_2 is close to the corresponding undamped subbranch in (a) when it exists. This explains why
 255 the experimental maximum steady-state wave elevations by Royon-Lebeaud et al. (2007) are satisfactory predicted by Faltinsen et al. (2016) within the framework of the undamped sloshing model.

The damping plays a significant role for the phase-lags. As we pointed out, the undamped sloshing is characterised by piecewise values of ψ and φ ,
 260 i.e., $\sin \psi = 0$ (φ is not defined) for planar and $\sin \psi = \cos \varphi = 0$ for swirling (along the response curves in figure 3 a). When $\xi > 0$, the phase-lags become complex functions and vary along the response curves, which, for planar waves, are determined in (35) but, for swirling, $C = \tan \alpha = \tan(\varphi - \psi) \geq 0$ (the inequality follows from the last equality of (36), in which $m_3 > m_1$) com-
 265 puted from the cubic equation (37). For swirling, ψ determines two different phase-lags $\varphi_1 = \psi + \alpha$ and $\varphi_2 = \psi + \alpha \pm \pi$, which imply two physically-identical angular waves occurring in clockwise and counterclockwise directions, respectively. Figure 4 shows ψ/π corresponding to the response curves in figure 3 (b). The graphs demonstrate that the phase-lag ψ is not a piece-
 270 wise function.

The non-constant phase-lag ψ was detected in experiments by Royon-Lebeaud et al. (2007) who quite logically concluded that this is due to the damping. Figure 5 compares their experimental data (circles) with theoretical predictions (swirling, the frequency range corresponds to the subbranch
 275 between H_1 and H_2 in figure 3 b); the theoretical curves are drawn for ξ from $\xi = \xi_1 = 0.005$ till $\xi = \xi_9 = 0.045$. Royon-Lebeaud et al. (2007) adopted a rigid circular base tank with $r_0 = 0.15$, $h = 1.5$ and the rather large forcing

amplitude $\eta_{1\alpha} = 0.045$. They reported strong wave breaking that means a non-negligible damping due to this free-surface phenomenon. As matter of fact, the boundary-layer and bulk viscosity effect (an estimate is $\xi_1 = 0.005$ by (10) and (11)) determines only a lower bound of the cumulative damping, i.e. $\xi \geq \xi_1$. Figure 5 confirms the latter fact. The theoretical curve (dashed line) with ξ_1 looks like an estimate from below of the experimental ψ -values. To fit the experimental ψ , one should assume that the cumulative damping rate ξ increases with increasing wave amplitude from H_1 to H_2 . This is consistent with the fact that the wave breaking becomes stronger with increasing the wave amplitude (Royon-Lebeaud et al., 2007).

As discussed by Miles (1984a,b), types of bifurcation points for the longitudinal forcing are similar to those appearing for the damped spherical pendulum (Miles, 1962). Readers who have an interests in what are the bifurcation points in Figs. 3 and 4 are therefore referred to Miles (1962, 1984a,b).

3.3. Elliptic tank excitations ($0 < \delta = \epsilon_y/\epsilon_x < 1$)

As we remarked above, the *undamped sloshing* due to the elliptic forcing is characterised by $\bar{a} = \bar{b} = 0$ (Faltinsen et al., 2016), which means $\sin \psi = \cos \varphi = 0$ and $\cos \alpha = 0$, $\sin \alpha = \pm 1$. As a consequence, [3] and [4] become identities, but $A = |a|$ and $B = |b|$ and [1] and [2] read as

$$A^2[\Lambda + m_1 A^2 + m_3 B^2] = \epsilon_x^2, \quad B^2[\Lambda + m_1 B^2 + m_3 A^2] = \delta^2 \epsilon_x^2. \quad (38)$$

This system with respect to A^2 and B^2 can be analytically solved as described in Faltinsen et al. (2016).

For *damped* sloshing with $\xi \neq 0$, the phase lags φ and ψ become rather complicated functions of the input parameters. Both A , B and φ , ψ should be found from the nonlinear system (33a). To exclude φ and ψ and decrease dimension of (33a), we insert $\varphi = \psi + \alpha$ into the right-hand sides of [2] and [4] and substitute $\epsilon_x \cos \psi$ and $\epsilon_x \sin \psi$ taken from [1] and [3]. The result is the following linear system of homogeneous equations

$$\begin{cases} (\delta A)[\cos \alpha(\mathcal{D}(C)B^2 + \xi) + \sin \alpha(\Lambda + m_1 A^2 + (m_3 - \mathcal{F}(C))B^2)] \\ \quad - B[\Lambda + m_1 B^2 + (m_3 - \mathcal{F}(C))A^2] = 0, \\ (\delta A)[\cos \alpha(\Lambda + m_1 A^2 + (m_3 - \mathcal{F}(C))B^2) - \sin \alpha(\mathcal{D}(C)B^2 + \xi)] \\ \quad - B[\mathcal{D}(C)A^2 - \xi] = 0, \end{cases}$$

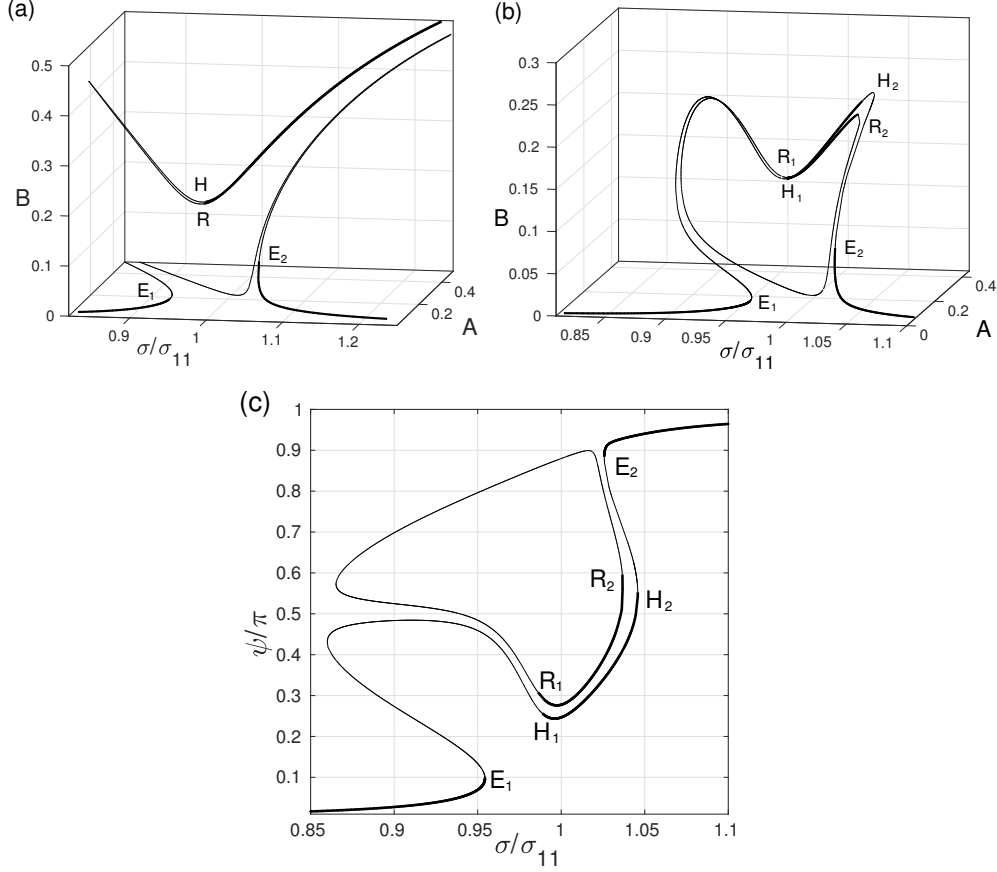


Fig. 6. Response curves for the steady-state resonant sloshing due to an elliptic counterclockwise periodic horizontal forcing with $\eta_{1a} = 0.01$, $\eta_{2a} = \delta\eta_{1a}$ and $\delta = 0.05$. The panel (a) corresponds to the undamped amplitude response curves ($\xi = 0$) but the panel (b) is drawn for $\xi = 0.02$. The panel (c) depicts ψ/π versus σ/σ_{11} . All response curves correspond to swirling but some subbranches in (a,b) are close to the $(\sigma/\sigma_{11}, A)$ -plane that means that sloshing behaves as an almost standing (planar) wave. The bold lines correspond to the stable sloshing. The branch in (b,c) containing E_1 , H_1 , and H_2, E_2 implies swirling, which co-directed with the elliptic forcing orbit but the loop-like branch with R_1 and R_2 marks the counter-directed swirling.

with respect to δA and B . The system must have a nontrivial solution. This leads to the zero-determinant condition

$$\xi(A^2 - B^2)\mathcal{D}(C) - \mathcal{F}(C)[\xi^2 + (\Lambda + m_1(A^2 + B^2))^2]/(m_3 - m_1) + A^2B^2\mathcal{D}^2(C) = 0, \quad (39)$$

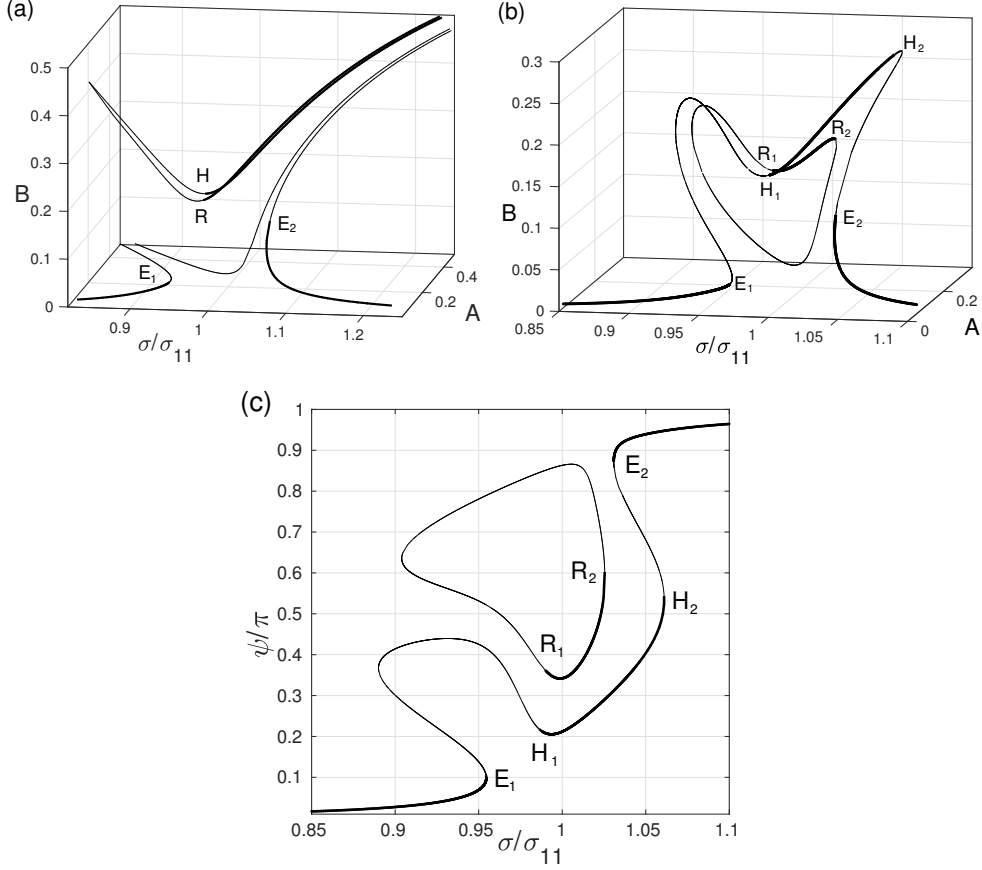


Fig. 7. The same as in figure 6 but for $\delta = \epsilon_y/\epsilon_x = 0.2$.

which couples A^2 , B^2 and C . Another two equations with respect to A^2 , B^2 and C come from $\boxed{1}^2 + \boxed{3}^2$ and $\boxed{2}^2 + \boxed{4}^2$ and take the form

$$\begin{cases} A^2[(\Lambda + m_1 A^2 + (m_3 - \mathcal{F})B^2)^2 + (\mathcal{D}B^2 + \xi)^2] = \epsilon_x^2, \\ B^2[(\Lambda + m_1 B^2 + (m_3 - \mathcal{F})A^2)^2 + (\mathcal{D}A^2 - \xi)^2] = \delta^2 \epsilon_x^2. \end{cases} \quad (40)$$

The system (39), (40) is a base for getting the response curves in the $(\sigma/\sigma_{11}, A, B)$ space. One can prove that $C \neq 0$ since $C = 0$ leads to (39) $\Rightarrow \xi^2 + (\Lambda + m_1(A^2 + B^2))^2 = 0$ and (40) $\Rightarrow A^2[\xi^2 + (\Lambda + m_1(A^2 + B^2))^2] = \epsilon_x^2 \neq 0$, simultaneously. Physically, $C \neq 0$ means that *there are no standing wave regimes* for the elliptic forcing. All steady-state sloshing regimes are *swirling*.

Our numerical experiments show that $C > 0$ as $(m_3 - m_1) > 0$. We do

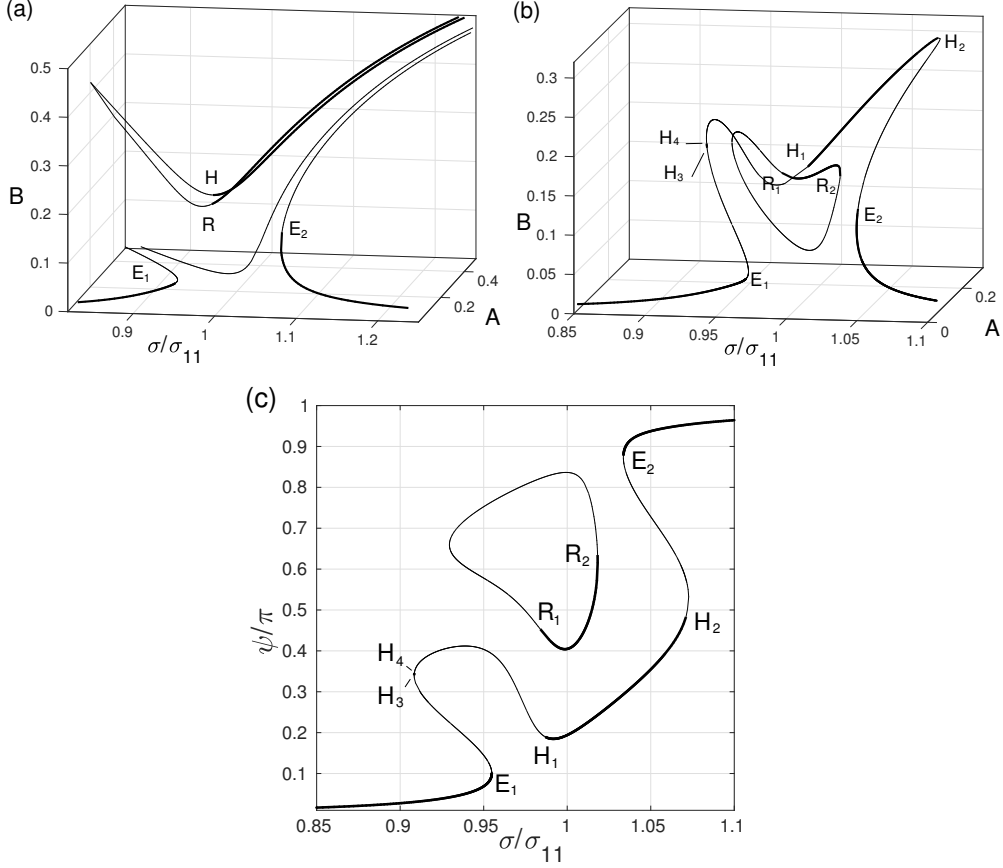


Fig. 8. The same as in figure 6 but for $\delta = \epsilon_y/\epsilon_x = 0.3$.

not know how to get an analytical solution of (39), (40). A numerical scheme is used. After defining \mathcal{F} and \mathcal{D} as functions of $0 < \beta < 1$,

$$\mathcal{F}(\beta) = (m_3 - m_1)\beta, \quad \mathcal{D}(\beta) = (m_3 - m_1) \sqrt{\beta(1 - \beta)}, \quad C > 0, \quad (41)$$

a simple analysis shows that

$$0 < A < \frac{\epsilon_x}{\xi}, \quad 0 < B^2 \leq \min \left[\frac{1}{\mathcal{D}(\beta)} \left(\frac{\epsilon_x}{A} - \xi \right), \frac{\delta^2 \epsilon_x^2}{(\mathcal{D}(\beta)A^2 - \xi)^2} \right], \quad (42)$$

which determines the fixed interval for A but the interval for B^2 is determined by A and β . The first equation of (40) computes the two real $\Lambda_{1,2}$ for any

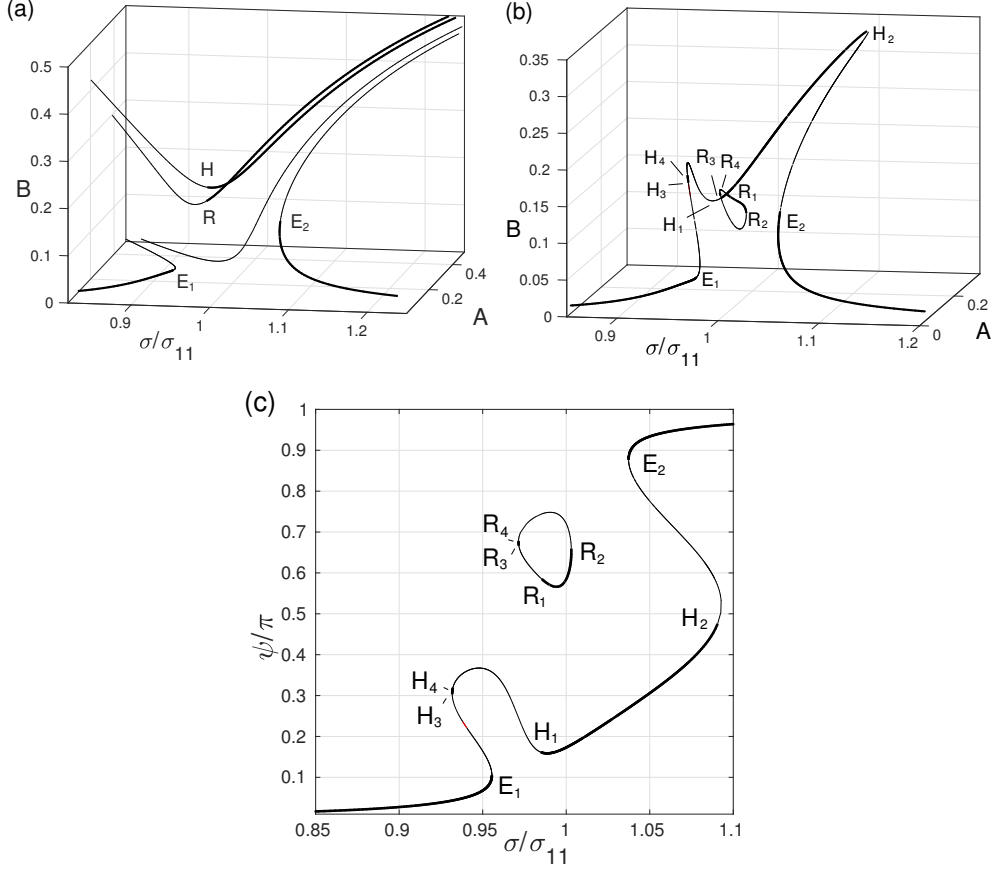


Fig. 9. The same as in figure 6 but for $\delta = \epsilon_y/\epsilon_x = 0.45$.

given $0 < \beta < 1$ and A, B^2 satisfying (42) as follows

$$\Lambda_{1,2} = -m_1 A^2 - (m_3 - \mathcal{F}(\beta)) B^2 \pm \sqrt{\frac{\epsilon_x^2}{A^2} - (\mathcal{D}(\beta) B^2 + \xi)^2}. \quad (43)$$

Furthermore, to solve (39), (40) for *any fixed* A belonging to the corresponding interval of (42)

- 1) we introduce a mesh $0 < \beta_1 < \beta_2 < \dots < \beta_k < \dots < \beta_K < 1$;
- 2) for any fixed $\beta_k \in \{\beta_n\}$, we solve the two equations (follow from the second equation of (40))

$$[\Lambda_j + m_1 B^2 + (m_3 - \mathcal{F}(\beta)) A^2]^2 + [\mathcal{D}(\beta) A^2 - \xi]^2 = \frac{\delta^2 \epsilon_x^2}{B^2}, \quad j = 1, 2, \quad (44)$$

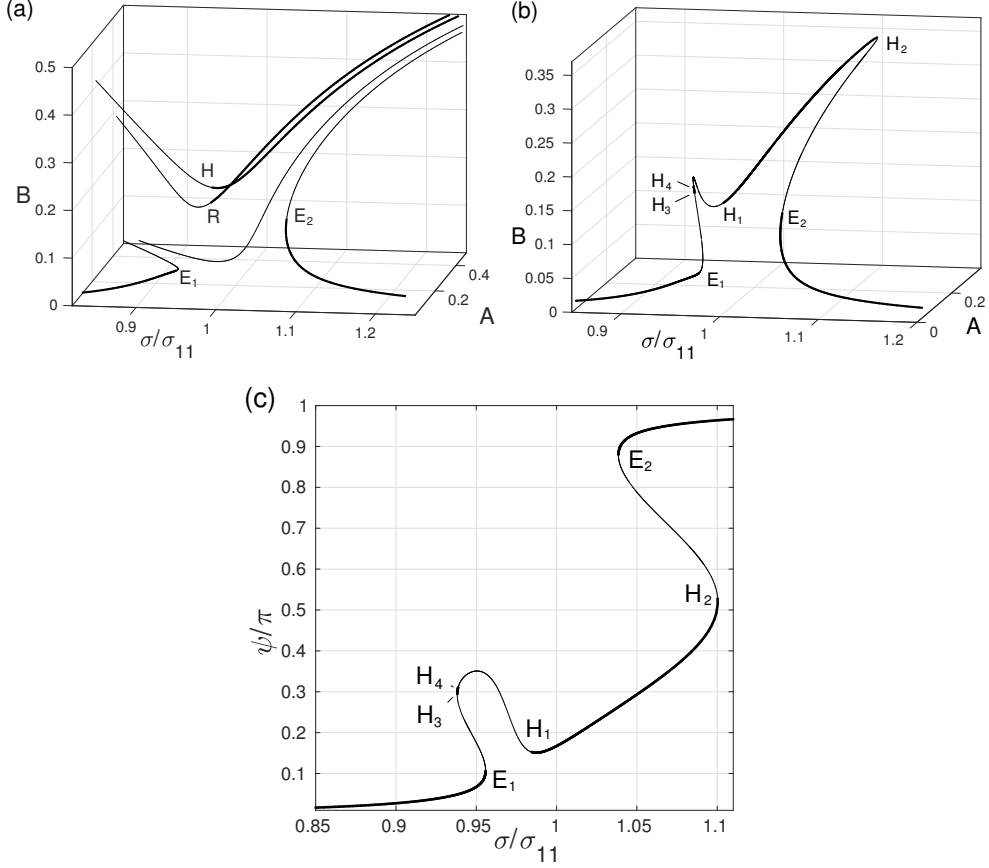


Fig. 10. The same as in figure 6 but for $\delta = \epsilon_y/\epsilon_x = 0.5$.

(associated with + and - in expression (43), respectively) with respect to B^2 on the interval by (42); the result is a set of positive roots $B_{k,j,i}^2 = B_i^2(A, \beta_k, j)$, $j = 1, 2$, for each A and β_k ;

305

3) each root $B_i(A, \beta_k, j)$ is subsequently substituted into (39):

$$\xi(A^2 - B_{i,k,j}^2)\mathcal{D}(\beta_k) - \mathcal{F}(\beta_k)[\xi^2 + (\Lambda_j + m_1(A^2 + B_{i,k,j}^2))^2]/(m_3 - m_1) + A^2 B_{i,k,j}^2 \mathcal{D}^2(\beta_k) = 0 \quad (45)$$

to detect the mesh interval (β_k, β_{k+1}) , where the left-hand side of (45) changes the sign;

4) an iterative procedure is used to compute $\beta \in (\beta_k, \beta_{k+1})$ and the corresponding $B_i(A, \beta, j)$.

310

The algorithm computes numerical solutions for any fixed A . Varying A in the interval by (42) outputs response curves in the $(\sigma/\sigma_{11}, A, B)$ space. The results are presented in figures 6–11 for several values of $0 < \delta < 1$.

Figure 6 illustrates changing the response curves in figures 3 and 4 due to a relatively small perturbation of ϵ_y , the ratio $\delta = \epsilon_y/\epsilon_x = 0.05$. This almost longitudinal horizontal forcing causes splitting the arc $PH_1H_2E_2$ in figure 3 (b), whose points determine two physically identical co- and counter-clockwise swirling waves, into two different branches. The first branch contains the points E_1, H_1, H_2, E_2 ; it exists far from the primary resonance zone, where the co-directed stable swirling wave is close to a standing planar wave. The corresponding subbranches are to the left of E_1 and to the right of the Poincaré bifurcation point E_2 . Another stability subbranch is H_1H_2 . The second loop-like branch with R_1 and R_2 implies swirling, which is counter-directed to the forcing. This swirling is stable on R_1R_2 . There is the frequency range between E_1 and H_1 where the theory does not predict any stable steady-state sloshing and irregular (chaotic) waves are expected.

Increasing the semi-axes ratio δ decreases the loop-like R branch responsible for the counter-directed swirling. Figures 7, 8 and 9 illustrate this fact. Decreasing the R -branch means that the linear damping makes the counter-directed swirling impossible when δ tends to 1. In contrast, the theoretical undamped analysis by Faltinsen et al. (2016) shows that the counter-directed propagating wave exists and may be stable in a frequency range for any $0 < \delta < 1$. The R branch disappears at a certain δ . When $\xi = 0.02$, this happens for δ slightly lower than 0.5. As a consequence, we do not see this branch in figure 10.

In figures 8–10, we also see extra islands of stability H_3H_4 and R_3R_4 . After the vanishing of the R branch, the island H_3H_4 grows, eventually connecting to stable subbranches.

Figure 11 shows what happens when the elliptic forcing orbit approaches a circular shape. Here, the difference between the undamped (a) and damped (b) cases is especially serious for both the amplitude (A, B) response curves and the phase-lag ψ . The damping allows (for any forcing frequency) only stable swirling, which is co-directed with the forcing. The corresponding branching has hard-spring type behaviour.

Even though our stability analysis method allows for classifying the types of bifurcation points in Figs. 6-11, we think that this classification should be subject of a dedicated paper. First, the present section has other goals, which are basically associated with estimating the stability ranges and types

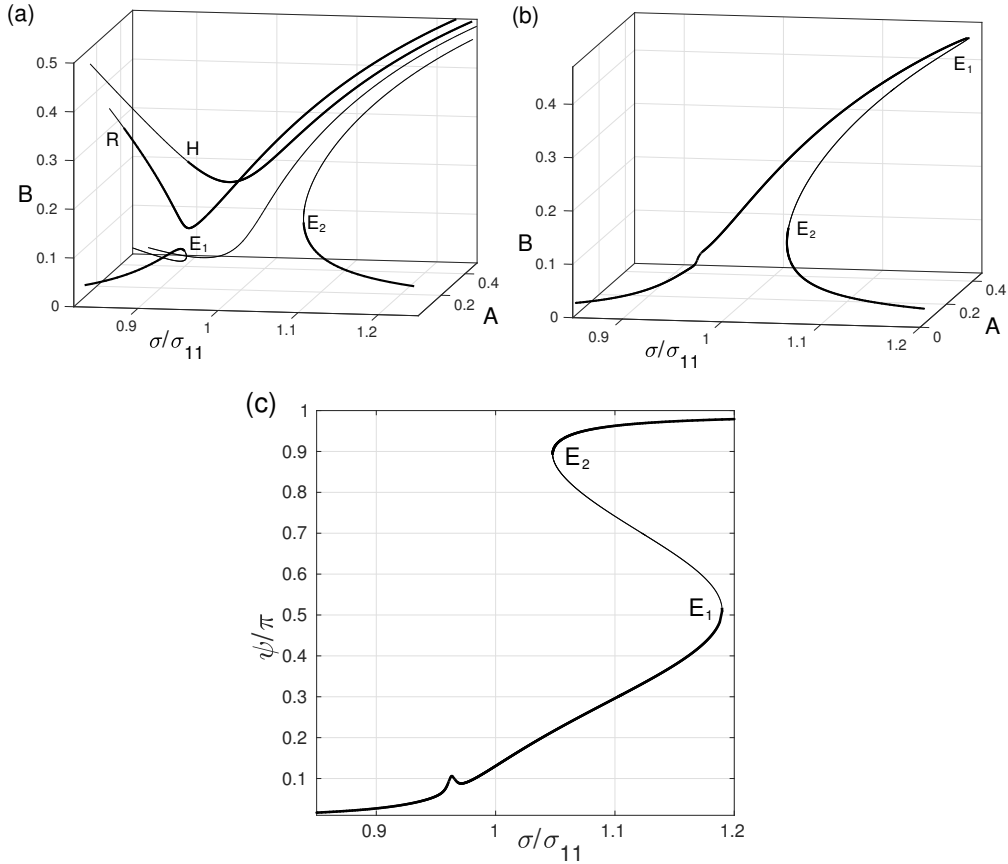


Fig. 11. The same as in figure 6 but for $\delta = \epsilon_y/\epsilon_x = 0.95$.

of swirling modes caused by the elliptic forcing. Secondly, our numerical tests showed that position of several bifurcation points in Figs. 6-11, e.g., associated with ‘local islands’ H_3H_4 may change with the forcing amplitude and the damping rate.

3.4. Rotary (circular) orbital forcing with $\delta = \epsilon_y/\epsilon_x = 1$

In the undamped case (Faltinsen et al., 2016), the rotary (orbital circular) forcing yields steady-state swirling in both angular directions. To study the damped sloshing by using the secular system (39), (40) with $\delta = 1$ and $\xi \neq 0$, we recall that $C \neq 0$ but the limit $C \rightarrow +\infty$ is possible. This limit implies the co-directed rotary wave. It transforms (39) to $A^2 = B^2$ and the two

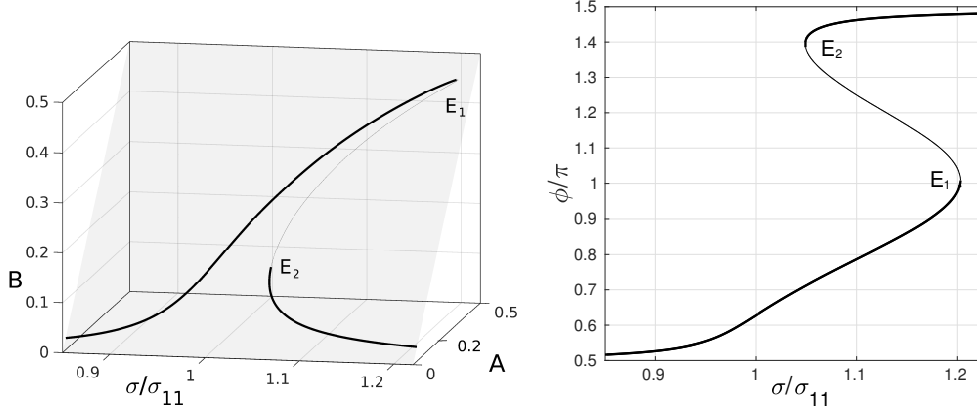


Fig. 12. The amplitude (A, B) and phase-lag (ψ) response curves for the rotary forcing ($\delta = 1$). The only co-directed (with circular forcing direction) swirling is possible and $A = B$. The amplitude demonstrates the hard-type spring behaviour, which is qualitatively confirmed by Reclari (2013) and Reclari et al. (2014).

equations (40) become equivalent

$$A = B > 0; \quad A^2(\Lambda + (m_1 + m_3)A^2)^2 + \xi^2 = \epsilon_x^2, \quad (46)$$

$\mathcal{D} = \mathcal{F} = 0$, that makes it possible to restore ψ and $\varphi - \psi = \pi/2$. Numerical
 355 experiments confirmed that (39), (40) with $\xi \neq 0$ have no solution except (46).

The corresponding response curves are illustrated in figure 12. They are
 360 qualitatively consistent with experimental data by Reclari (2013) (unfortunately, the experiments were done with the lower liquid depth, $h = 1.04$, when the Narimanov-Moiseev-type modal equations have a limited applicability due to the secondary resonance). The wave-amplitude branching has the hard-spring type behaviour that is also consistent with the experiments.

4. Conclusions and discussion

The nonlinear multimodal theory by Faltinsen et al. (2016) is modified
 365 by adding linear damping terms, which reflect the linear damping rates (responsible for the logarithmic decrements) of the natural sloshing modes. The damping rates express a cumulative effect of diverse dissipative sources including the boundary layer at the wetted tank surface and the bulk viscosity. The damping rates may significantly increase when the dynamic contact angle, free-surface contamination, wave breaking, etc. matter. The
 370

latter increase typically happens for laboratory tanks (bioreactors). The original multimodal theory neglects surface tension (for tap water, the tank radius $r_0 \gtrsim 0.05$ cm) and assumes that the circular base container performs a prescribed periodic sway/surge/pitch/roll motion with the forcing frequency close to the lowest natural sloshing frequency; the mean liquid depth-to-the tank radius ratio is $h \gtrsim 1.2$ to avoid the secondary resonance phenomena.

The asymptotic steady-state solution of the modal equations is derived. Its stability is analysed by using the linear Lyapunov method and the multi-timing technique. The asymptotic procedure introduces two dominant, lowest-order wave amplitudes and related phase-lags, which are governed by four (secular) nonlinear algebraic equations. These equations have the same structure as if the container performs an elliptic horizontal translatory orbital motion. This makes possible to concentrate on the steady-state wave regimes occurring due to these elliptic excitations with different semi-axes ratios δ . The longitudinal horizontal harmonic tank forcing and the circular (rotary) forcing are two limiting cases.

The undamped and damped steady-state sloshing due to longitudinal horizontal harmonic forcing leads to either planar or swirling waves. Introducing the linear damping leads to extra bifurcation points on the amplitude response curves where swirling emerges from the planar wave regime. Each point on the swirling-related branch implies two physically identical but counter-directed progressive angular waves. For a non-zero δ , the branching splits into two disconnected curves, one of which corresponds to swirling, which is co-directed with the forcing, but the other implies a counter-directed swirling. Increasing the semi-axes ratio makes the second response curve (counter-directed swirling) decrease until it finally vanishes at a certain δ . This is opposite to the undamped case (Faltinsen et al., 2016), when the counter-directed swirling was co-existing for any $0 < \delta \leq 1$.

A focus has been on the phase-lag, which is a piecewise constant function along the amplitude response curves in the undamped case, but it becomes of the non-constant character when the damping is not zero. A comparison is done with measurements of the phase-lag by Royon-Lebeaud et al. (2007) (longitudinal forcing) to show that, if the damping rates are associated with the boundary layer at the wetted tank surface and the bulk viscosity, a satisfactory agreement for lower wave amplitudes can be achieved but the cumulative damping must be larger to fit the experiments with increasing the wave amplitude. The reason is a strong wave breaking reported by Royon-Lebeaud et al. (2007). For elliptic excitations with relatively small semi-

axes ratio, the theory detects a frequency range where no stable steady-state
410 solutions exist. For the longitudinal case, expected wave patterns, including
chaotic ones, are extensively simulated and discussed by Miles (1984a,b) and
Ikeda et al. (2012). What happens for elliptic excitations needs a dedicated
study.

For the circular (rotary) orbital forcing, the amplitude response curves
415 have the hard-spring type behaviour. That is qualitatively consistent with
observations and measurements by Reclari (2013) and Reclari et al. (2014).

While the resonant wave patterns occurring due to longitudinal excita-
tions are well analysed and visualised by using the multimodal theories (see,
e.g., Gavriluk et al., 2000), a question whether the present theory could
420 play the same role for elliptic excitations appears. The authors think that
this question deserves a dedicated study.

The presented modified theory cannot describe the mean vortical flow (a
mean liquid rotation around the container axis) reported in experiments by
Prandtl (1949), Hutton (1964), Royon-Lebeaud et al. (2007), Reclari (2013),
425 Reclari et al. (2014), Bouvard et al. (2017). In part, the latter phenomenon
can be explained by the angular Stokes drift (Faltinsen and Timokha, 2009,
Sect. 9.6.3). One must consider a viscous rotational flow model to quantify
it in a mathematical way. The effect of viscosity, in general, and the bound-
ary layer force, in particular, can correct the potential flow description and,
430 moreover, affect the stability results as it is reported by Vega et al. (2001),
Knobloch et al. (2002) and Martin et al. (2002).

Acknowledgements

The second author acknowledges a financial support of the Centre of
Autonomous Marine Operations and Systems (AMOS) whose main sponsor
435 is the Norwegian Research Council (Project number 223254-AMOS).

Appendix A. Nonlinear terms of the modal equations (14)-(17)

$$\begin{aligned}
\mathcal{P}_{11}(p_{11}, r_{11}; p_{0j}, p_{2j}, r_{2j}) &= d_1 p_{11} (\ddot{p}_{11} p_{11} + \ddot{r}_{11} r_{11} + \dot{p}_{11}^2 + \dot{r}_{11}^2) \\
&\quad + d_2 [r_{11} (\ddot{p}_{11} r_{11} - \ddot{r}_{11} p_{11}) + 2\dot{r}_{11} (\dot{p}_{11} r_{11} - \dot{r}_{11} p_{11})] \\
&\quad + \sum_{j=1}^{I_r} \left[d_3^{(j)} (\ddot{p}_{11} p_{2j} + \ddot{r}_{11} r_{2j} + \dot{p}_{11} \dot{p}_{2j} + \dot{r}_{11} \dot{r}_{2j}) + d_4^{(j)} (\ddot{p}_{2j} p_{11} + \ddot{r}_{2j} r_{11}) \right. \\
&\quad \left. + d_5^{(j)} (\ddot{p}_{11} p_{0j} + \dot{p}_{11} \dot{p}_{0j}) + d_6^{(j)} \ddot{p}_{0j} p_{11} \right], \quad (\text{A.1a})
\end{aligned}$$

$$\begin{aligned}
\mathcal{R}_{11}(p_{11}, r_{11}; p_{0j}, p_{2j}, r_{2j}) &= d_1 r_{11} (\ddot{p}_{11} p_{11} + \ddot{r}_{11} r_{11} + \dot{p}_{11}^2 + \dot{r}_{11}^2) \\
&\quad + d_2 [p_{11} (\ddot{r}_{11} p_{11} - \ddot{p}_{11} r_{11}) + 2\dot{p}_{11} (\dot{r}_{11} p_{11} - \dot{p}_{11} r_{11})] \\
&\quad + \sum_{j=1}^{I_r} \left[d_3^{(j)} (\ddot{p}_{11} r_{2j} - \ddot{r}_{11} p_{2j} + \dot{p}_{11} \dot{r}_{2j} - \dot{p}_{2j} \dot{r}_{11}) + d_4^{(j)} (\ddot{r}_{2j} p_{11} - \ddot{p}_{2j} r_{11}) \right. \\
&\quad \left. + d_5^{(j)} (\ddot{r}_{11} p_{0j} + \dot{r}_{11} \dot{p}_{0j}) + d_6^{(j)} \ddot{p}_{0j} r_{11} \right], \quad (\text{A.1b})
\end{aligned}$$

$$\mathcal{P}_{2k}(p_{11}, r_{11}) = d_{7,k} (\dot{p}_{11}^2 - \dot{r}_{11}^2) + d_{9,k} (\ddot{p}_{11} p_{11} - \ddot{r}_{11} r_{11}), \quad (\text{A.2a})$$

$$\mathcal{R}_{2k}(p_{11}, r_{11}) = 2d_{7,k} \dot{p}_{11} \dot{r}_{11} + d_{9,k} (\ddot{p}_{11} r_{11} + \ddot{r}_{11} p_{11}) = 0, \quad (\text{A.2b})$$

$$\mathcal{P}_{0k}(p_{11}, r_{11}) = d_{8,k} (\dot{p}_{11}^2 + \dot{r}_{11}^2) + d_{10,k} (\ddot{p}_{11} p_{11} + \ddot{r}_{11} r_{11}); \quad (\text{A.2c})$$

$$\begin{aligned}
\mathcal{P}_{3k}(p_{11}, r_{11}; p_{0j}, p_{2j}, r_{2j}) &= d_{11,k} [\ddot{p}_{11} (p_{11}^2 - r_{11}^2) - 2p_{11} r_{11} \ddot{r}_{11}] \\
&\quad + d_{12,k} [p_{11} (\dot{p}_{11}^2 - \dot{r}_{11}^2) - 2r_{11} \dot{p}_{11} \dot{r}_{11}] + \sum_{j=1}^{I_r} \left[d_{13,k}^{(j)} (\ddot{p}_{11} p_{2j} - \ddot{r}_{11} r_{2j}) \right. \\
&\quad \left. + d_{14,k}^{(j)} (\ddot{p}_{2j} p_{11} - \ddot{r}_{2j} r_{11}) + d_{15,k}^{(j)} (\dot{p}_{2j} \dot{p}_{11} - \dot{r}_{2j} \dot{r}_{11}) \right], \quad (\text{A.3a})
\end{aligned}$$

$$\begin{aligned}
\mathcal{R}_{3k}(p_{11}, r_{11}; p_{0j}, p_{2j}, r_{2j}) &= d_{11,k} [\ddot{r}_{11}(p_{11}^2 - r_{11}^2) + 2p_{11}r_{11}\ddot{p}_{11}] \\
&+ d_{12,k} [r_{11}(\dot{p}_{11}^2 - \dot{r}_{11}^2) + 2p_{11}\dot{p}_{11}\dot{r}_{11}] + \sum_{j=1}^{I_r} \left[d_{13,k}^{(j)} (\ddot{p}_{11}r_{2j} + \ddot{r}_{11}p_{2j}) \right. \\
&\quad \left. + d_{14,k}^{(j)} (\ddot{p}_{2j}r_{11} + \ddot{r}_{2j}p_{11}) + d_{15,k}^{(j)} (\dot{p}_{2j}\dot{r}_{11} + \dot{r}_{2j}\dot{p}_{11}) \right]; \quad (\text{A.3b})
\end{aligned}$$

$$\begin{aligned}
\mathcal{P}_{1n}(p_{11}, r_{11}; p_{0j}, p_{2j}, r_{2j}) &= d_{16,n}(\ddot{p}_{11}p_{11}^2 + r_{11}p_{11}\ddot{r}_{11}) \\
&+ d_{17,n}(\ddot{p}_{11}r_{11}^2 - r_{11}p_{11}\ddot{r}_{11}) + d_{18,n}p_{11}(\dot{p}_{11}^2 + \dot{r}_{11}^2) + d_{19,n}(r_{11}\dot{p}_{11}\dot{r}_{11} - p_{11}\dot{r}_{11}^2) \\
&\quad + \sum_{j=1}^{I_r} \left[d_{20,n}^{(j)} (\ddot{p}_{11}p_{2j} + \ddot{r}_{11}r_{2j}) + d_{21,n}^{(j)} (p_{11}\ddot{p}_{2j} + r_{11}\ddot{r}_{2j}) \right. \\
&\quad \left. + d_{22,n}^{(j)} (\dot{p}_{11}\dot{p}_{2j} + \dot{r}_{11}\dot{r}_{2j}) + d_{23,n}^{(j)} \ddot{p}_{11}p_{0j} + d_{24,n}^{(j)} p_{11}\ddot{p}_{0j} + d_{25,n}^{(j)} \dot{p}_{11}\dot{p}_{0j} \right], \quad (\text{A.4a})
\end{aligned}$$

$$\begin{aligned}
\mathcal{R}_{1n}(p_{11}, r_{11}; p_{0j}, p_{2j}, r_{2j}) &= d_{16,n}(\ddot{r}_{11}r_{11}^2 + r_{11}p_{11}\ddot{p}_{11}) \\
&+ d_{17,n}(\ddot{r}_{11}p_{11}^2 - r_{11}p_{11}\ddot{p}_{11}) + d_{18,n}r_{11}(\dot{p}_{11}^2 + \dot{r}_{11}^2) + d_{19,n}(p_{11}\dot{p}_{11}\dot{r}_{11} - r_{11}\dot{p}_{11}^2) \\
&\quad + \sum_{j=1}^{I_r} \left[d_{20,n}^{(j)} (\ddot{p}_{11}r_{2j} - \ddot{r}_{11}p_{2j}) + d_{21,n}^{(j)} (p_{11}\ddot{r}_{2j} - r_{11}\ddot{p}_{2j}) + d_{22,n}^{(j)} (\dot{p}_{11}\dot{r}_{2j} - \dot{r}_{11}\dot{p}_{2j}) \right. \\
&\quad \left. + d_{23,n}^{(j)} \ddot{r}_{11}p_{0j} + d_{24,n}^{(j)} r_{11}\ddot{p}_{0j} + d_{25,n}^{(j)} \dot{r}_{11}\dot{p}_{0j} \right], \quad n = 2, \dots, I_r, \quad (\text{A.4b})
\end{aligned}$$

where the nondimensional hydrodynamic coefficients are functions of h (Faltinsen et al., 2016).

Appendix B. Stability analysis by the linear Lyapunov method

The linear Lyapunov method and the multi-timing technique is employed to study stability of the constructed asymptotic steady-state solution. This procedure suggests introducing the slowly varying time $\tau = \frac{1}{2}\epsilon^{2/3}t$ and expressing the perturbed solutions as

$$\begin{aligned}
a_1 &= (a + \alpha(\tau)) \cos t + (\bar{a} + \bar{\alpha}(\tau)) \sin t + o(\epsilon^{1/3}), \\
b_1 &= (\bar{b} + \bar{\beta}(\tau)) \cos t + (b + \beta(\tau)) \sin t + o(\epsilon^{1/3}),
\end{aligned} \quad (\text{B.1})$$

where a, \bar{a}, b and \bar{b} come from (28). Inserting (B.1) into the modal equations, gathering terms of the lowest asymptotic quantities order and keeping linear terms in $\alpha, \bar{\alpha}, \beta$ and $\bar{\beta}$ lead to the following linear system of ordinary differential equations

$$\mathbf{s}' + \xi \mathbf{s} + \mathcal{S} \mathbf{s} = 0, \quad (\text{B.2})$$

where $\mathbf{s} = (\alpha, \bar{\alpha}, \beta, \bar{\beta})^T$, the prime is the differentiation by τ , and the matrix \mathcal{S} has the following elements

$$\begin{aligned} s_{11} &= -2m_1 a \bar{a} - (m_1 - m_3) b \bar{b}; & s_{13} &= -2m_1 \bar{a} b - (m_1 - m_3) a \bar{b}, \\ s_{12} &= -(\bar{\sigma}_{11}^2 - 1) - m_1(a^2 + 3\bar{a}^2 + b^2) - m_3 \bar{b}^2; & s_{14} &= -2m_3 \bar{a} \bar{b} - (m_1 - m_3) a b, \\ s_{21} &= (\bar{\sigma}_{11}^2 - 1) + m_1(3a^2 + \bar{a}^2 + \bar{b}^2) + m_3 b^2; & s_{22} &= 2m_1 a \bar{a} + (m_1 - m_3) b \bar{b}, \\ s_{23} &= 2m_3 a b + (m_1 - m_3) \bar{a} \bar{b}; & s_{24} &= 2m_1 \bar{a} b + (m_1 - m_3) a \bar{b}, \\ s_{31} &= 2m_1 \bar{a} b + (m_1 - m_3) b \bar{a}; & s_{32} &= 2m_3 \bar{a} \bar{b} + (m_1 - m_3) a b, \\ s_{33} &= 2m_1 b \bar{b} + (m_1 - m_3) a \bar{a}; & s_{34} &= (\bar{\sigma}_{11}^2 - 1) + m_1(b^2 + 3\bar{b}^2 + a^2) + m_3 \bar{a}^2, \\ s_{41} &= -2m_3 a b - (m_1 - m_3) \bar{a} \bar{b}; & s_{42} &= -2m_1 \bar{a} b - (m_1 - m_3) a \bar{b}, \\ s_{43} &= -(\bar{\sigma}_{11}^2 - 1) - m_1(3b^2 + \bar{b}^2 + \bar{a}^2) - m_3 a^2; & s_{44} &= -2m_1 b \bar{b} - (m_1 - m_3) a \bar{a}. \end{aligned}$$

The fundamental solution $\mathbf{s} = \exp(\lambda \tau) \mathbf{a}$ of (B.2) follows from the spectral matrix problem $[(\lambda + \xi)I + \mathcal{S}] \mathbf{a} = 0$, where λ are the unknown eigenvalues, \mathbf{a} are the corresponding eigenvectors and I is the identity matrix. Computations give the following characteristic biquadratic equation

$$(\lambda + \xi)^4 + s_1(\lambda + \xi)^2 + s_0 = 0, \quad (\text{B.3})$$

440 where s_0 is the determinant of \mathcal{S} and s_1 is a complicated function of the elements of \mathcal{S} . The eigenvalues λ can be expressed as $-\xi \pm \sqrt{x_{1,2}}$, where $x_{1,2} = \frac{1}{2}(-s_1 \pm \sqrt{s_1^2 - 4s_0})$ are two solutions of the quadratic equation $x^2 + s_1 x + s_0 = 0$. The fixed-point solution (associated with a, \bar{a}, b and \bar{b}) is asymptotically stable ($\alpha, \bar{\alpha}, \beta$ and $\bar{\beta}$ exponentially decay with τ) if and only
445 if the real component of λ is strictly negative.

In the limiting case $\xi \rightarrow 0$, the stability condition ($\Re[\lambda] < 0$) takes the following form

$$s_1^2 - 4s_0 \geq 0 \quad \& \quad s_0 \geq 0 \quad \& \quad s_1 \geq 0. \quad (\text{B.4})$$

For $O(\epsilon^{2/3}) = \xi > 0$, the stability condition can be written as the alter-

native

$$\begin{aligned} & \text{either } s_1^2 - 4s_0 \geq 0 \ \& \ -s_1 + \sqrt{s_1^2 - 4s_0} \leq 0 \quad (\Leftrightarrow s_0 \geq 0 \ \& \ s_1 \geq 0), \\ & \text{or } s_1^2 - 4s_0 \geq 0 \ \& \ -s_1 + \sqrt{s_1^2 - 4s_0} > 0 \ \& \ \sqrt{\frac{1}{2} \left(-s_1 + \sqrt{s_1^2 - 4s_0} \right)} < \xi, \\ & \text{or } s_1^2 - 4s_0 < 0 \ \& \ \sqrt{2\sqrt{s_0} - s_1} < \xi. \end{aligned} \tag{B.5}$$

Barnyak, M., Leschuk, O., 2008. Construction of solutions of the problem of free oscillations of viscous fluid in a half-filled spherical tank. *Nonlinear Oscillations* 11, 461–483.

450 Bouvard, J., Herreman, W., Moisy, F., 2017. Mean mass transport in an orbitally shaken cylindrical container. *Physical Review Fluids* 2, 084801: 1–17.

Ducci, A., Weheliye, W.H., 2014. Orbitally shaken bioreactors-viscosity effects on flow characteristics. *AIChE Journal* 60, 3951–3968.

455 Faltinsen, O.M., Lukovsky, I.A., Timokha, A.N., 2016. Resonant sloshing in an upright annular tank. *Journal of Fluid Mechanics* 804, 608–645.

Faltinsen, O.M., Timokha, A.N., 2009. *Sloshing*. Cambridge University Press, Cambridge.

460 Faltinsen, O.M., Timokha, A.N., 2017. Resonant three-dimensional nonlinear sloshing in a square-base basin. Part 4. Oblique forcing and linear viscous damping. *Journal of Fluid Mechanics* 822, 139–169.

Gavrilyuk, I., Lukovsky, I., A.N.Timokha, 2000. A multimodal approach to nonlinear sloshing in a circular cylindrical tank. *Hybrid Methods in Engineering* 2, 463–483.

465 Hutton, R.E., 1964. Fluid-particle motion during rotary sloshing. *Journal of Applied Mechanics, Transactions ASME* 31, 145–153.

Ikeda, T., Ibrahim, R.A., Harata, Y., Kuriyama, T., 2012. Nonlinear liquid sloshing in a square tank subjected to obliquely horizontal excitation. *Journal of Fluid Mechanics* 700, 304–328.

- 470 Keulegan, G., 1959. Energy dissipation in standing waves in rectangular basins. *Journal of Fluid Mechanics* 6, 33–50.
- Kim, H.M., Kizito, J., 2009. Stirring free surface flows due to horizontal circulatory oscillation of a partially filled container. *Chem. Eng. Comm.* 196, 1300–1321.
- 475 Knobloch, E., Martel, C., Vega, J.M., 2002. Coupled mean flow-amplitude equations for nearly inviscid parametrically driven surface waves. *Annals of the New York Academy of Sciences* 974, 201–219.
- Lukovsky, I., A.N.Timokha, 2017. Multimodal method in sloshing. *Journal of Mathematical Sciences* 220, 239–253.
- 480 Martel, A., Nicolás, J.A., Vega, J.M., 1998. Surface-wave damping in a brimful circular cylinder. *Journal of Fluid Mechanics* 360, 213–228.
- Martin, E., Martel, C., Vega, J.M., 2002. Drift instability of standing faraday waves. *Journal of Fluid Mechanics* 467, 57–79.
- Miles, J., 1962. Stability of forced oscillations of a spherical pendulum. *Quarterly of Applied Mathematics* 20, 21–32.
- 485 Miles, J., 1984a. Internally resonant surface waves in circular cylinder. *Journal of Fluid Mechanics* 149, 1–14.
- Miles, J., 1984b. Resonantly forces surface waves in circular cylinder. *Journal of Fluid Mechanics* 149, 15–31.
- 490 Miles, J., 1994. Faraday waves: rolls versus squares. *Journal of Fluid Mechanics* 269, 353–371.
- Miles, J.W., Henderson, D.M., 1998. A note on interior vs. boundary-layer damping of surface waves in a circular cylinder. *Journal of Fluid Mechanics* 364, 319–323.
- 495 Prandtl, L., 1949. Erzeugung von Zirkulation beim Schütteln von Gefässen. *ZAMM* 29, 8–9.
- Reclari, M., 2013. Hydrodynamics of orbital shaken bioreactors. Thesis no 5759 (2013). *École Polytechnique Federale de Lausanne*.

- Reclari, M., Dreyer, M., Tissot, S., Obreschkow, D., Wurm, F.M., Farhat, M., 2014. Surface wave dynamics in orbital shaken cylindrical containers. *Physics of Fluids* 26, 1–11.
500
- Royon-Lebeaud, A., Hopfinger, E., Cartellier, A., 2007. Liquid sloshing and wave breaking in circular and square-base cylindrical containers. *Journal of Fluid Mechanics* 577, 467–494.
- Shukhmurzaev, Y., 1997. Moving contact lines in liquid/liquid/solid systems. *Journal of Fluid Mechanics* 334, 211–249.
505
- Vega, J.M., Knobloch, E., Martel, C., 2001. Nearly inviscid faraday waves in annular containers of moderately large aspect ratio. *Physica D* 154, 313–336.
- Weheliye, W., Yianneskis, M., Ducci, A., 2013. On the fluid dynamics of shaken bioreactors – flow characterization and transition. *AIChE* 59, 334–344.
510